Marina do Carmo Alves

**$Cu(In,Ga)Se_2$ thin film solar cell
by magnetron sputtering**

outubro de 2018

$Cu(In,Ga)Se_2$ thin film solar cell by magnetron sputtering
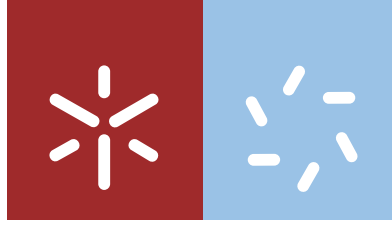
Marina do Carmo Alves

UMinho | 2018

Universidade do Minho
Escola de Ciências

Marina do Carmo Alves

**Cu(In,Ga)Se$_2$ thin film solar cell
by magnetron sputtering**

Dissertação de Mestrado
Mestrado em Ciências e Tecnologias do Ambiente
Ramo Energia

Trabalho realizado sob orientação do
Doutor João Pedro dos Santos Hall Agorreta Alpuim
e do
Doutor Sascha Sadewasser

outubro de 2018

DECLARAÇÃO

Nome: Marina do Carmo Alves

Endereço eletrónico: marina.dcalves@gmail.com   **Telefone:** 935938325

Cartão do Cidadão: 18019529

Título da dissertação: Cu(In,Ga)Se$_2$ thin film solar cell by magnetron sputtering

Orientadores:

Doutor João Pedro dos Santos Hall Agorreta Alpuim

Doutor Sascha Sadewasser

Ano de conclusão: 2018

Designação do Mestrado: Mestrado em Ciências e Tecnologias do Ambiente – Ramo Energia

É AUTORIZADA A REPRODUÇÃO PARCIAL DESTA DISSERTAÇÃO, APENAS PARA EFEITOS DE INVESTIGAÇÃO, MEDIANTE DECLARAÇÃO ESCRITA DO INTERESSADO, QUE A TAL SE COMPROMETE.

Universidade do Minho, 31 / 08 / 2018

Assinatura: *Marina do Carmo Alves*

Acknowledgements

Abstract

The purpose of this thesis is to develop a deposition processes for $Cu(In,Ga)Se_2$ by DC magnetron sputtering to be employed as an absorber layer in $Cu(In,Ga)Se_2$-based photovoltaic devices. The thesis describes three deposition processes: (1) co-deposition of Cu, In, Ga and Se, where Cu, In and Ga are sputtered and Se is evaporated at the same time, (2) Cu, In, Ga deposition by sputtering followed by post-selenization and (3) a pulsed deposition of Cu, In, Ga by sputtering and Se by evaporation.

A calibration of the CuInGa precursor and the Se source were performed, involving several experiments such as varying the Ar flow, applied power and substrate temperature in order to determine the influence on the film and establish the best deposition parameters.

For the three processes, the $Cu(In,Ga)Se_2$ layer was deposited onto soda lime glass (SLG) substrate coated with a molybdenum layer. The samples produced were characterized by scanning electron microscopy (SEM) for surface morphology, energy-dispersive X-ray spectroscopy (EDX) for chemical composition, stylus profilometry and/or cross-sectional SEM analysis for thickness and X-ray diffraction (XRD) for structure identification.

The $Cu(In,Ga)Se_2$ co-deposition resulted in tetragonal CIGS, as revealed by XRD. The CuInGa deposition with post-selenization and the $Cu(In,Ga)Se_2$ pulsed deposition resulted in Cu-rich $Cu(In,Ga)Se_2$ films, which are not desired, hence these two techniques are considered unsuitable for the CIGS deposition process. A solar cell was fabricated for each deposition process and an efficiency of 1.57% was achieved for the co-deposition solar cell.

Keywords: CIGS, Thin film, Solar cell, Sputtering.

Resumo

Esta tese teve como objetivo desenvolver um processo de deposição de Cu(In,Ga)Se$_2$ por *DC sputtering* para ser utilizado como camada absorsora em dispositivos fotovoltaicos de Cu(In,Ga)Se$_2$. Três processo de deposição são descritos nesta tese: (1) co-deposição de Cu, In, Ga, Se, onde Cu, In e Ga são depositados por *sputtering* e o Se é evaporado simultaneamente, (2) deposição de Cu, In e Ga por *sputtering* seguido de pós-selenização e (3) deposição pulsada de Cu, In e Ga por *sputtering* e evaporação de Se.

Foi necessário realizar a calibração do precursor CuInGa e da fonte de Se, portanto diversas experiências foram realizadas variando-se o fluxo de Ar, a potência aplicada e a temperatura do substrato com o objetivo de determinar a influência no filme e estabelecer os melhores parâmetros a serem utilizados na deposição.

Nos três processos, a camada absorsora foi depositada em substrado de vidro soda-cal revestido com uma camada de molibdênio. As amostras produzidas foram caracterizadas por microscopia eletrónica de varrimento (MEV) para avaliar a morfologia da superfície, espectroscopia de dispersão de raios-X (EDX) para avaliar composição química, perfilômetro e/ou seção transversal no MEV para determinar espessura e difração de raios-X (DRX) para identificação da estrutura.

A co-deposição de Cu(In,Ga)Se$_2$ resultou na presença de CIGS tetragonal atrvés do DRX. A deposição de CuInGa seguida de pós-selenização e a deposição pulsada de CIGS resultaram em filmes de Cu(In,Ga)Se$_2$ ricos em cobre, portanto essas duas técnicas são consideradas inadequadas para a deposição de Cu(In,Ga)Se$_2$. Para cada processo de deposição foi fabricada uma célula solar, e uma eficiência de 1,57% foi alcançada na célula solar produzida pelo processo de co-deposição.

Palavras-chave: CIGS, Filme fino, Célula solar, *sputtering*.

Table of Contents

List of Figures

List of Tables

1. Introduction

Nowadays, the world greatest environmental challenge is the sustainable development, expressly, the use and substitution of traditional energy sources for renewable ones. The development of clean energy resources as an alternative to traditional sources, especially to fossil fuels, has become one of the most important tasks assigned to modern science and technology in the 21st century [1]. It is known that fossil fuels are considered finite because they are not formed in the same proportion as their use, and the existing stocks require new technologies for their extraction. Another concern, is the emissions from fossil fuel use, which have significantly increased the concentration of green-house gases. Although several energy sources are used for power generation, the power generation from fossil fuel emits tons and tons of carbon dioxide (CO_2) and other dangerous gases such as SO_X and NO_X, causing environmental damages and risks to public health [2].

Energy is intertwined in every aspect of society lives and economy, since it changes, improves and raises life quality and is used for several segments as transportation, products manufacturing, heating, electricity, etc. Energy demand is directly related to population growth, thus higher the population growth rate, greater the energy demand, and to meet this demand, it is necessary to use other resources to generate more power, especially electric power. Electrical energy is constantly/uninterruptedly used to supply basic needs and those related to the comfort and well-being of the population. Without energy the whole fabric of society as we know it would crumble, the effect of a 24 hours cut in the electricity supplies to a city shows how totally dependent we are [3]. Therefore, the direct connection between renewable energy and sustainable development is undeniable, and by using these sources properly, it is possible to move towards a safe and sound environment [2].

Sustainable development demands a sustainable supply of energy resources that, in the long term, is readily and sustainably available at reasonable cost and can be utilized for all required tasks without causing negative impacts, as well as an effective and efficient utilization of energy sources [3]. Within all renewable energy sources, solar energy has a substantial potential and most of the renewable energies rely on the sunlight directly or indirectly [2], since the amount of energy supplied by the sun to the earth is more than five orders of magnitude larger than the world electric power consumption to keep modern civilization going [1].

In order to harvest and utilize the light and heat energy generated by the Sun, different technologies are required. These technologies can be classified in (1) passive solar technologies, which involves the accumulation of solar energy without transforming thermal or light energy into any other form and (2) active solar technologies, where a system collects solar radiation and uses mechanical and electrical equipment for the conversion of solar energy to heat and electric power [4]. The photovoltaic technology is a type of active solar technology that uses a semiconductor to convert sunlight into electricity.

Several materials can be used in the manufacture of solar cells, the mostly known and commercialized are the ones made from crystalline silicon. Currently, the research for new technologies has intensified and thin film solar cells have become more attractive since they are less material resulting in a more environmentally friendly and low-cost production. The copper indium gallium diselenide (CIGS) solar cells are considered promising alternative crystalline silicon solar cells due to their comparable efficiency (~23%) and their manufacturing cost, which can be reduced substantially by using inexpensive substrate (glass) [5]. This thesis is focused on the development of a deposition process of $Cu(In,Ga)Se_2$ (CIGS) layer by sputtering at the Sputtering for Advanced Research (STAR) system to be used as absorber material in thin film solar cells.

2. Theory

2.1. Solar Cells

Solar cell devices are able to transform solar radiation into electricity by the photovoltaic effect, which is generally defined as the emergence of an electric voltage between two electrodes attached to a solid or liquid system upon shining light onto the system [6]. The photovoltaic effect was discovered by Edmond Becquerel in 1839 but the first theory of a solid state device was developed a century later, in 1940 by Mott and Schottky [7]. Then, in 1954, the first silicon solar cell was developed with an efficiency of 6% and in 1958 solar cells were used on a satellite [7]. Due to the oil crisis in 1973, the limitations of fossil fuels were evident, as the need for development and research on alternative energy sources.

Solar cells, also known as photovoltaic devices, can be divided in three generations. The first generation consist in traditional solar cells made from crystalline silicon, which corresponds to more than 80% of solar cells produced [8].

Second generation solar cells, also known as thin films solar cells, are single-junction devices that aim to use less material and still achieve high efficiencies to compete with the first generation solar cells. This generation includes three types of solar cells: amorphous silicon (a-Si), cadmium telluride (CdTe) and copper indium gallium diselenide (CIGS).

The third generation aims to achieve high efficiency devices, while maintaining the economic and environmental cost advantages of thin film deposition techniques [9] and includes multijunction/heterojunction tandem cells, intermediate band cells, multi-exciton generation cells and hot carrier cells [10].

An ideal solar cell material must comply with six requirements: (1) bandgap between 1.1 and 1.7 eV, (2) direct bandgap structure, (3) consist in readily available, non-toxic materials, (4) easy, reproducible deposition technique, suitable for large area production, (5) good photovoltaic conversion efficiency and (6) long-term stability [6].

2.2.1. The p-n junction

Photovoltaic devices, incorporate a p-n junction in a semiconductor across which the photovoltage is developed [6], thus, the photovoltaic cells consist of a junction between two layers of semiconductor materials, n-type and p-type, resulting in a heterojunction for different

semiconductor materials, or a homojunction for similar semiconductors with different doping. The main concern with heterojunction devices is the difference in the electronic affinity between the materials, which will cause discontinuities in the structure of the energy bands.

Photovoltaic power generation occurs when electrons absorbing quanta from incoming radiation (light) are excited from the valence band (most energetic occupied band) into the next unoccupied band, called conduction band, allowing the material to conduct electricity [10] (Fig. 2.1). When a photon is absorbed by an electron in the valence band, the absorbed energy excites the electron to the conduction band where it can move freely, leaving an empty state in the valence band where the electron was placed [11]. The bandgap of a semiconductor is a decisive parameter, in an ideal case, no photons with energy lower than the bandgap will contribute to photogeneration, whereas all photons with energy higher than the bandgap will each contribute to the photogenerated electron-hole pair, with the excess energy being very rapidly lost by thermalization [8]. In the n-type layer, the semiconductor material is doped with atoms with an extra electron, whereas in the p-type layer, the dopant atoms don't have enough electrons, leaving free spots or holes in the valence band. When the p-n junction is formed, the electrons will diffuse from one layer to another, creating a depletion region that acts as an internal electric field leading to the separation of photo excited electron-hole pairs.
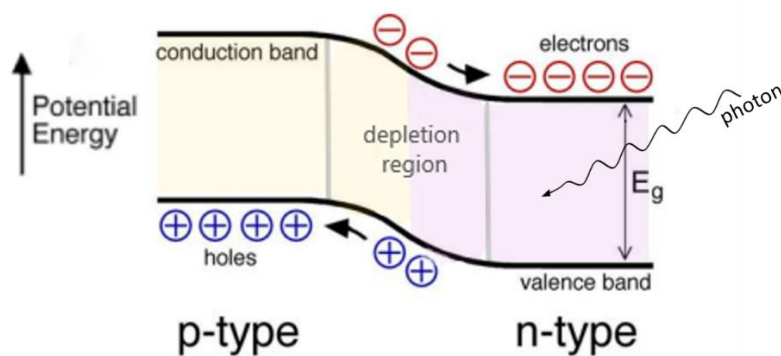
Figure 2.1 - Band diagram of a p-n junction (adapted from [12]).

The CIGS solar cell consists in a heterojunction, formed with the p-type CIGS absorber layer and the n-type CdS (or Zn(O,S)) and ZnO layers. The incoming light with energy higher than the CIGS bandgap is mainly absorbed within the first micrometer of the absorber layer, creating electron-hole pairs [13]. Due to a built-in electric field across the p-n junction interface, electrons within the diffusion length region are swept away from the p-type absorber to the n-type buffer layer

and collected by the n-type electrode, similarly, holes are swept away from the n-type layer to the p-type layer and collected by the p-type electrode [5].

Figure 2.2 shows a schematic band diagram of a CIGS solar cell under zero-bias voltage condition, where the Mo back contact is covered with the CIGS absorber layer, which has an average bandgap energy about 1.2 eV, the n-type CdS buffer layer has a bandgap of around 2.4 eV, while the i-ZnO and Al:ZnO layers have a wide bandgap over 3 eV [13]. Therefore, the p-n junction formed between the p-type layer and the n-type layer causes the bending of the valence and conduction bands [13].
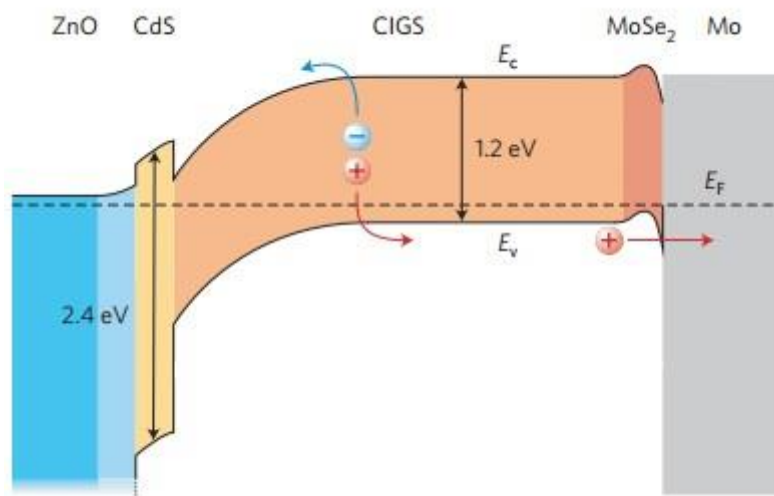
Figure 2.2 - Schematic band diagram of a CIGS solar cell under zero-bias voltage condition [adapted from 13]

In any structure, solar cells, which are connected in series and in parallel in order to form the desired voltage and current levels, remain the basic semiconductor components of a photovoltaic panel. The primary solar cell equivalent circuit is modeled as a current source with a parallel diode [7]. From a typical solar cell I-V curve (Fig. 2.3), parameters such as short-circuit current (I_{sc}), open-circuit voltage (V_{oc}), electrical power delivered by the cell at the maximum power point (Pmax), fill factor (FF) can be analyzed [8]. The most important factor of merit in a photovoltaic module is efficiency (η), defined as:

$$\eta = \frac{FF \times V_{oc} \times I_{sc}}{P_{in}}$$

where P_{in} (W/m^2) represents the incident power and is defined by the solar irradiance per area times the area of the solar cell.
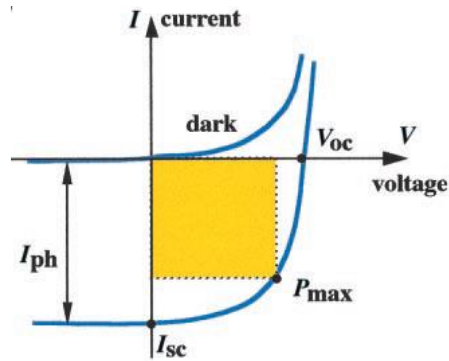
Figure 2.3 - Typical current-voltage curve of a solar cell [8].

2.2.2. Thin-film solar cells

Thin film solar cells consist in the deposition of several layers of different materials, where the thickness of these layers are a few micrometers. Thus, it has the potential for substantial cost advantage when compared to crystalline wafers due to a lower material use, fewer processing steps, and simple device processing and manufacturing technology for large-area modules and arrays [14]. However, the first objective is to achieve a high efficiency, then the choice of any technology will be dictated by the highest achievable efficiency, easy manufacturing, reliability, availability of materials, and environmental sensitivity [14]. Among the various thin film technologies, amorphous silicon (a-Si), cadmium telluride (CdTe) and copper indium gallium selenide (CIGS) are the most widely commercialized solar cells.

Amorphous silicon solar panels have shown relatively low efficiencies, thus, they are not as promising for large scale. However, a-Si solar cells are widely used in the technology industry for calculators, watches, etc [15].

Cadmium telluride solar cells are an ideal material for thin-film photovoltaics because it has an optimum bandgap ($\sim$1.45 eV) with a high absorption coefficient and the deposition process is considered easy and simple to handle [6]. Laboratory cells and commercial modules have achieved efficiency higher than 22.1% and 18.6%, respectively [15]. The main concern regarding CdTe is the Cd toxicity, which during the module production has environmental hazard and safety issues. However, as a compound, CdTe is stable and probably nontoxic [8]. CIGS solar cells have been intensively researched, since they can be deposited with different methods, have very high optical absorption and laboratory efficiencies exceed 22.4% [5] [16]. However, the main concern regarding CIGS, is the use of In, which is a less abundant and expensive material [17]. With the large

production of CIGS modules, the In demand may increase, leading to a price escalation due to a supply-demand gap [5].

2.3. CIGS thin film structure

The CIGS solar cell consists in a heterogeneous p-n junction, and can be divided in three main groups: back contact, absorber layer and window layer. The device structure essentially is substrate/Mo/CIGS/CdS/i-ZnO/ZnO:Al (Fig. 2.4). The bottom is usually a glass substrate followed by a molybdenum back contact. On top of the Mo layer is the absorber layer, $Cu(In,Ga)Se_2$, this p-type semiconductor film absorbs most of the light and generates the photocurrent. The heterojunction is formed by depositing a very thin n-type buffer layer, commonly CdS is used, however, alternative materials such as Zn(O,S) are being investigated. An intrinsic zinc oxide layer lies on top of the CdS and finally, the ZnO:Al layer functions as the front contact. The thickness of the semiconductor used in thin film solar cell varies from 1.2 to 4.04 µm, which is very thin compared to the crystalline silicon at 170-200 µm [15].
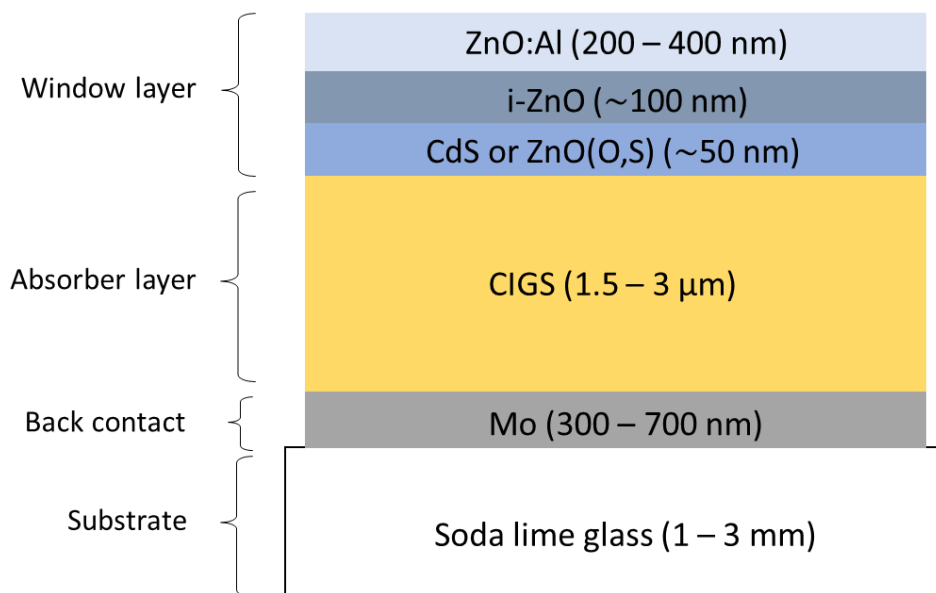
Figure 2.4 – Schematic of a typical CIGS solar cell structure.

Substrate and Back Contact

The substrate is a passive component in the device and is required to be mechanically stable, matching thermal expansion coefficient with deposited layers and inert during the device fabrication. The substrate has two types of configuration, (1) In the substrate configuration, light enter the cell through the window layer, more specific, through the front contact or transparent

conductive oxide layer, and at the (2) superstrate configuration, light enters the cell through a glass substrate, which acts as a window for illumination [5]. The substrate seems to play an active role in improving the photovoltaic performance of the CIGS absorber materials [18]. The most common substrate is soda lime glass (SLG), but several materials can be used such as flexible substrates. The use of SLG as substrate has been widely used since Na diffuses from the substrate to the CIGS absorber layer through the Mo layer and in a moderate level, improves cell efficiency [5]. The beneficial effects of Na incorporation include the improvement of film morphology, V_{OC} and FF [5] and It also reduces the defect concentration of the absorber films [19].

For the back contact, Mo is used because of it is relatively inert during the highly corrosive CIGS deposition conditions [18] and it also acts as a reflector and reflects unused light back into the absorber [5]. The adhesion of Mo films to the substrate and the sheet resistivity is highly dependent on the sputter conditions [18] thence a bilayer process is used and the deposition occurs by DC sputtering.

CIGS Absorber layer

The absorber layer is the most important layer since its function is essentially to absorb sunlight and convert it into electrons and holes. The CIGS absorber layer is used as the p-type material that forms the p-n junction and it is an alloy formed by the mixture of $CuInSe_2$ and $CuGaSe_2$. A more detailed analysis of the CIGS properties and deposition methods are presented in section 2.3 and 2.4, respectively.

Window layer

The primary function of a window layer in a heterojunction is to form a junction with the absorber layer while admitting a maximum amount of light to the junction region and absorber layer [18]. The window layer can be divided in three sub-layers: buffer layer, shunt preventing layer and transparent conductive oxide layer.

The buffer layer is used as the n-type material that forms the p-n junction in the solar cell. The CIGS solar cells typically use a CdS buffer layer, deposited by chemical bath deposition (CBD) process, which are widely used as an interfacial layer in order to improve the efficiency [19]. However, several alternative window layers are being investigated, such as Zn(O,S), which is

normally deposited by a chemical bath deposition (CBD) process, to replace CdS due to the Cd toxicity. Efficiencies higher than 18% have been reported using a Zn(O,S) buffer layer [5].

On top of the buffer layer, a bilayer of zinc oxide is what forms the proper window layer and must be highly transparent, with a bandgap of approximately 3.3 eV. The first layer is thin intrinsic (undoped) zinc oxide (i-ZnO), which provides an isolation between the buffer layer and the transparent conductive oxide layer, preventing the diffusion of Al into the absorber layer [5] and is also used to protect the buffer and the absorber layer from ion damage during the ZnO:Al sputtering [20], since the latter is usually deposited by RF sputtering, known as a damaging process. The second layer, called transparent conductive oxide (TCO) layer, works as a front contact for the cell, allowing the passage and collection of the current and it is chosen based on their conductivity, transparency, moisture stability and compatibility with further processing. The most commonly material used as a TCO layer is aluminum doped zinc oxide (ZnO:Al).

2.4. CIGS absorber layer properties

$CuInSe_2$ and $CuGaSe_2$ are the compounds that form the alloy $Cu(In,Ga)Se_2$ (CIGS), which belongs to the I-III-VI$_2$ group of chalcopyrites that crystallizes in the tetragonal chalcopyrite structure (Fig 2.5) and is the basis for one of the most promising photovoltaic technologies. The CIGS compound has desirable features as absorber in the thin film solar cells, such as a direct band gap and specifically high optical absorption coefficient that makes the chalcopyrite compounds well suited for thin film solar cells [21].
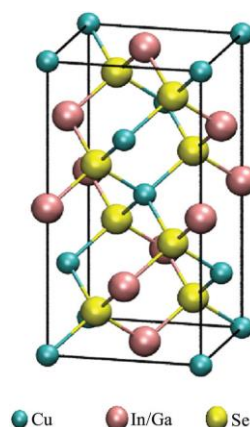
● Cu   ● In/Ga   ● Se

Figure 2.5 - Crystal structure of a tetragonal chalcopyrite CIGS unit cell [5].

CIGS is a promising absorber material due to its direct bandgap ranging from $CuInSe_2$, with a bandgap of 1.04 eV, to $CuGaSe_2$ with a bandgap of 1.7 eV.

The composition ratio for the CIGS films has a strong influence on the performance of the cell, especially the [Cu]/([In]+[Ga]) ratio and the [Ga]/([In]+[Ga]) ratio in the film. High efficiencies of over 10% are obtained in a relative wide range of [Cu]/[III] ratios from 0.75 to 0.95, when the ratio is higher than 0.95, the devices do not show any photovoltaic effect [19]. The Ga composition ratio [Ga]/[III] is typically 0.2 - 0.3 and a further increase of the Ga composition ratio usually degrades the cell efficiency [19]. The incorporation of Ga will raise the bandgap of the material and the V_{oc}, thus, if all indium is replaced by Ga, the CIGS bandgap increases about 1.7 eV [5]. Record efficiency devices were produced with an average bandgap of 1.1 - 1.2 eV, which corresponds to a [Ga]/([In]+[Ga]) ratio of approximately 0.3 [20]. In addition, the incorporation of Ga also improves the adhesion of the Mo back contact.

The presence of Na in the CIGS layer, also improves the cell efficiency. During the CIGS growth on SLG substrates at high temperatures, Na diffuses through the Mo layer from the SLG substrate to the CIGS layer by thermal activation. Therefore, as mentioned, the incorporation of Na in a moderate level (0.1 at%) improves the efficiency and film morphology [5].

Due to the amount of elements and compounds involved in the formation of CIGS, the growth of the film is extremely complex due to the difficulties in controlling the composition and maintaining stoichiometry. Therefore, a pseudobinary Cu_2Se-In_2Se phase diagram (Fig.2.6) can be used to identify CIS different phases [21]. A typical Cu content of device-quality CIGS varies from 22 to 24 at% Cu, which correspond to the α-phase ($CuInSe_2$) at growth temperature of 500-550°C. At room temperature, it is very complex to obtain $CuInSe_2$, since the Cu content varies between 24 and 24.5 at% Cu [21]. It turns out that the partial replacement of In with Ga, along with the use of Na-containing substrates, widens the single phase region in terms of (In+Ga)/(In-Ga-Cu) ratios [21].
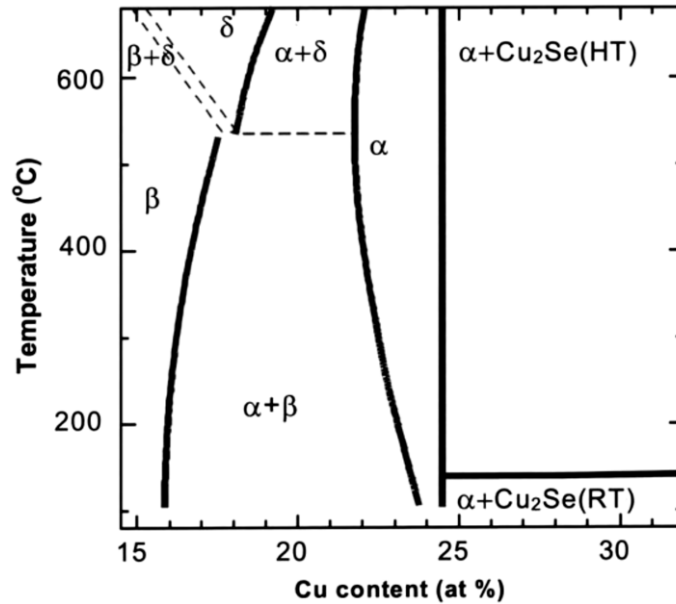
Figure 2.6 – Pseudobinary cut Cu$_2$Se-In$_2$Se of the ternary phase diagram that comprises all ternary Cu-in-Se compounds [21]

2.5. CIGS absorber layer deposition

CIGS thin films can be prepared by a wide range of methods, thus, suitable deposition methods with efficiency, low-cost, reproducibility and control are highly essential [22] .

Although several methods can be used, three methods dominate the production, (1) co-evaporation, (2) sequential deposition and (3) non-vacuum techniques. The co-evaporation technique has become a standard because it leads to highly efficient solar cells [23] and can be categorized by the number of growth stages in which elements are deposited under vacuum as thin layers at different deposition rates and substrate temperatures [5]. The second method consist in a two-stage deposition process where the metal precursors are sputtered followed by selenization and/or sulfurization [23]. To select the deposition technique, it is necessary to consider the production scale. For lab-scale production the focus is precise control over CIGS film composition and cell efficiency. For industrial production, criteria such as reproducibility, cost, high-throughput and process tolerance are also essential [5].

2.5.1. Sputtering

Sputtering is a physical vapor deposition (PVD) technique used to deposit thin films and was first observed in a DC gas discharge tube by Grove in 1852. Several sputtering systems are used for the deposition of thin films, such as ion beam, DC diode, RF diode, cylindrical magnetron, planar magnetron. Among these sputtering systems, the basic model is the DC diode sputtering system.

The DC sputtering system is composed of a pair of planar electrodes, one of the electrodes is cathode and the other is anode. The power supply is a high-voltage DC source, the sputtering target is the cathode of the discharge and the anode usually is the substrate [24] (Fig.2.7).
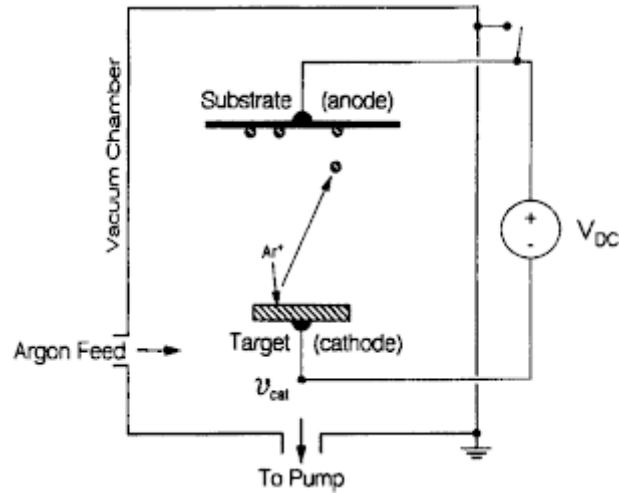
Figure 2.7 - Schematic of a DC sputtering system [24].

The DC sputtering process is carried out in an evacuated chamber which is backfilled with a low pressure inert gas, usually argon (Ar). Then, a DC voltage is applied to the cathode (target), which breaks down the Ar gas to form a glow discharge consisting of Ar^+ ions and electrons. The energetic ions are accelerated to bombard the target, ejecting target atoms which are deposited on the substrate, forming a coating.

The advantage of sputtering is that the chamber gets heat up relatively low comparing with other techniques and the deposition can easily be controllable by plasma current. The loss is minimum in the film which means that the composition of the film is more or less the same as the target [25]. The deposition rates of sputtering systems are lower than those of vacuum deposition, however, lowering the sputtering pressure increases the deposition rates [25].

Sometimes, gases or gas mixtures other than Ar are used. Usually, this involves some sort of reactive sputtering process in which a compound is synthesized by sputtering a metal target in a reactive gas to form a compound of the metal and the reactive gas species [26]. Therefore, reactive sputtering is a method to deposit films which have a different composition from the target by adding a gas to the sputtering system to produce a reaction of the gas with the target material [27] and can be defined by the reaction between atoms sputtered from a metal target and reactive gas molecules diffused from a discharge gas on the substrate to produce compound thin films [28].

22

The reactive sputtering usually requires the use of a reactive gas, such as H_2Se [29], which is a toxic gas.

3. Experimental Techniques

3.1. Sputtering System STAR (Sputtering for Advanced Research)

Sputtering for Advanced Research (STAR) (Fig 3.1) is a sputtering system design and built for the deposition of thin films by DC or RF sputtering. It is a homemade system developed in cooperation with the Institute of Micro and Nanotechnology (IMN), in Spain. The system consists in three interconnected vacuum chambers, each one with its own pumping system, at a working pressure of $1x10^{-7}$ mbar.
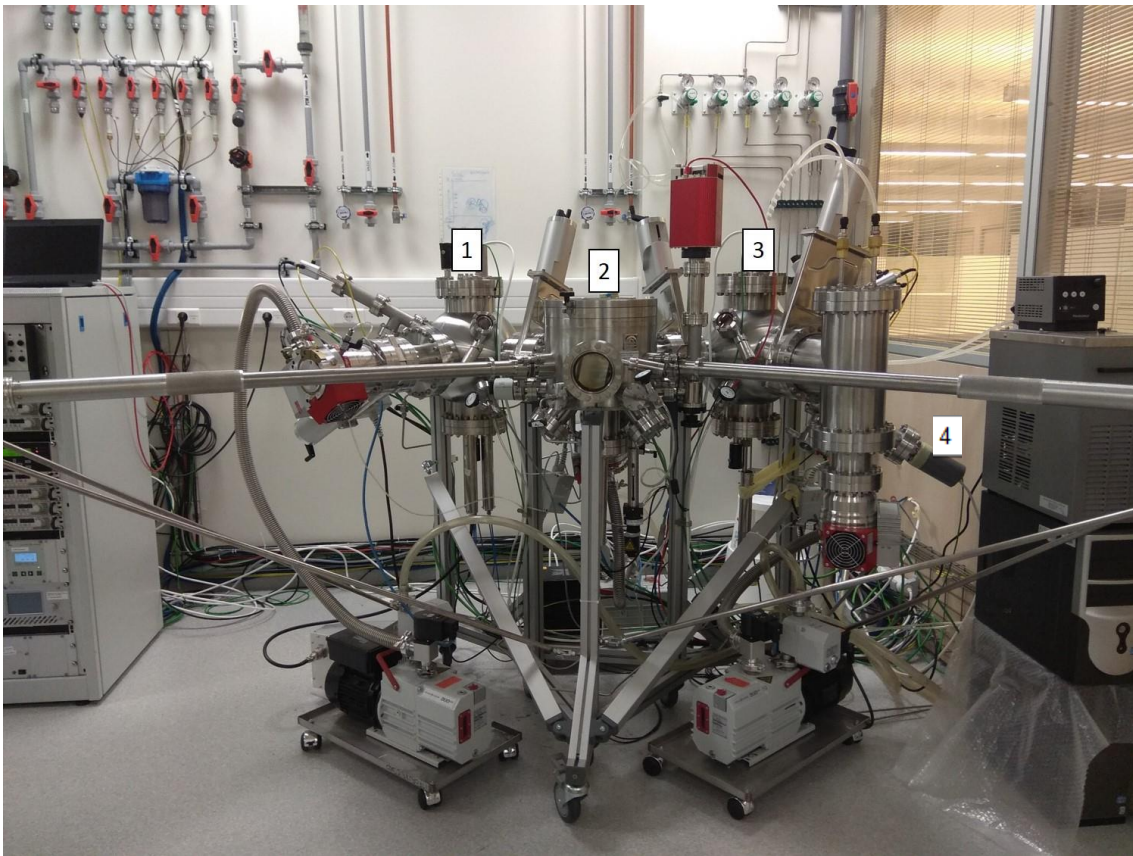
Figure 3.1 - Sputtering for Advanced Research – STAR. (1) Window chamber, (2) Loading chamber, (3) CIGS chamber and (4) Se Source.

The loading chamber has two main functions, it is where the samples are loaded and can be transferred to the others chambers and where the molybdenum deposition by DC sputtering is done. At the CIGS chamber, copper, indium, gallium are deposited by DC sputtering and selenium by evaporation. It's possible to mount and use up to three targets, which was the initial configuration (copper, indium and indium/gallium targets). The most recent configuration has only one target, a composite target with CuInGa (50:35:15 at%). At the CIGS chamber also a Selenium

source is mounted. The Window Chamber is where the window layers are deposited by RF sputtering. It has three targets, intrinsic zinc oxide (i-ZnO), zinc oxide doped with aluminum (ZnO:Al) and zinc oxide sulfide (Zn(O,S)), and it is the only chamber with an oxygen line. All chambers have argon and nitrogen lines, quartz crystal balance, pressure sensor and cooling water connected to each magnetron. A schematic of the STAR system is represented in Fig 3.2.
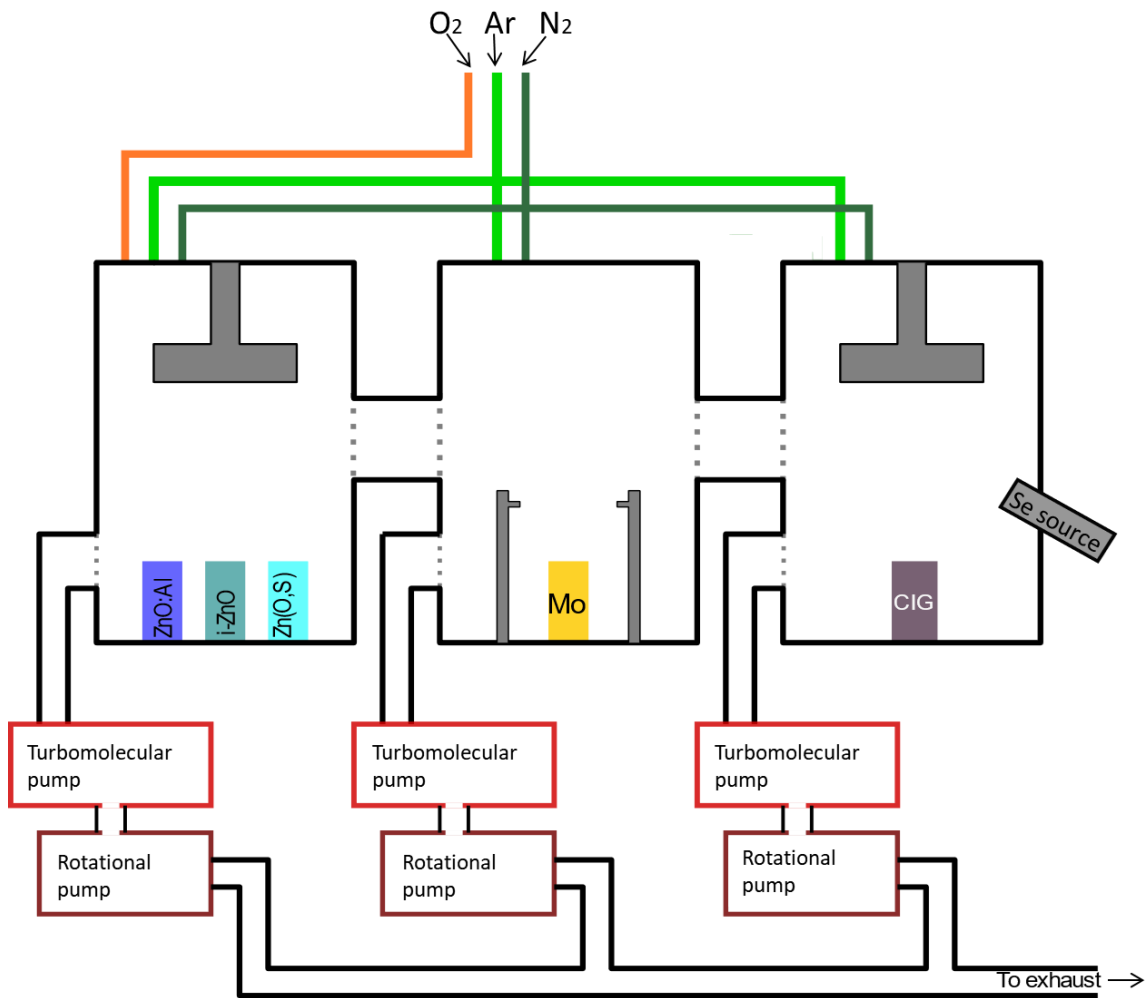
Figure 3.2 - Schematic of the STAR system

It is important to highlight that all CIGS deposition processes in STAR were initiated in this study, from calibration to actual deposition.

3.1.1. Shutter

Shields and shutters are used for preconditioning and protect targets and/or substrates. To minimize their effect on ion neutralization, they should be made as symmetric as possible with respect to the target and the materials from which shields and shutters are constructed are also important to avoid contamination of targets and/or films [26].

Two shutters were built at CIGS chamber to protect the targets from contamination, the first one is designed to be used with three targets configuration and the second one, for a single target (Fig 3.3).
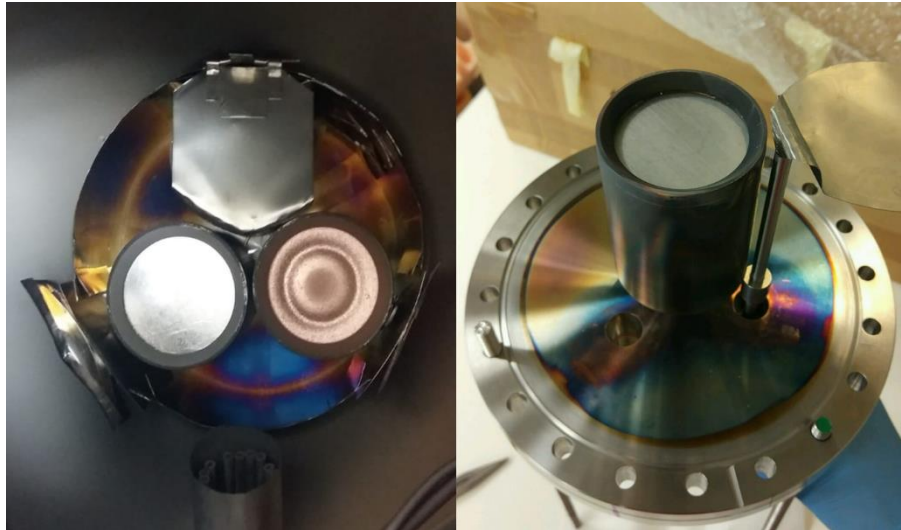
Figure 3.3 – Shutters built to protect the targets. Configuration with three targets (left) and one target (right).

3.1.2. Se source and selenization process

The Se source was installed during the research work for this thesis and consists in a Se cell where Se pellets (approximately 100g) were placed to provide Se vapor, a Se cracker that thermally breaks up evaporated large Se molecules and a Se valve that closes the Se exit to the chamber and can be used to control the flow by varying the Se valve opening (V_{Se}). Since Se gas is corrosive, a cooling system was also mounted in order to prevent any pump damage. Figure 3.4 shows a schematic of the Se source.
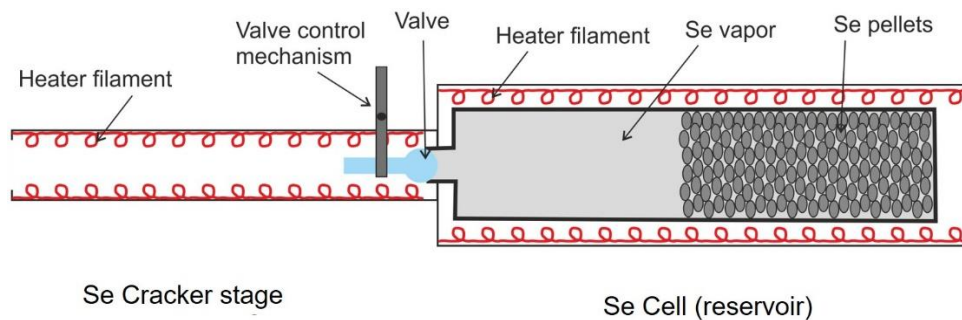
Figure 3.4 - Schematic of the Se source.

A Se source was installed at STAR to allow the performance of different methods and process. For all process with selenium, it is necessary to heat the Se source. The first step is to start the water-cooling system, until it reaches 5°C. Then, the Se cell is heated to 300 °C at a rate of 30 °C/min

followed by the Se cracker at 45% (84 W), which corresponds to an applied power of 84 W and temperature of 595°C (see Section 4.3).

When the deposition process is concluded, a final step is required when the substrate is heated. To prevent Se loss, the Se valve (V_{Se}) is kept open during the substrate cooling until the temperature reaches 270 °C.

3.1.3. Sputtering process

During the thesis, Mo, Cu, In, CuInGa ($Cu_{0.5}In_{0.35}Ga_{0.15}$) were sputter deposited. To initiate the sputtering it is necessary to ignite the plasma in the chamber. Therefore, a higher Ar flow is introduced into the chamber to raise the pressure up to a desired value, then, the DC power supply is turned on in order to ignite the plasma. Sometimes, to ignite the magnetron it was necessary to increase the pressure by slightly closing the pump valve.

Prior to the deposition, a pre-sputtering is required to clean the targets and to adjust the parameters to the desired ones in which will occur the deposition. As the pre-sputtering occurs, the sample is inside the chamber, protected by the shutter. During this work, to initiate the plasma an Ar flow of 90 sccm (standard cubic centimeters per minute) was used for all targets. In Table 3.1 all the parameters used for the pre-sputtering are indicated.

Table 3.1 - Pre-sputtering parameters for each target (Mo, Cu, In and CuInGa).

Target	Ar (sccm)	Current (A)	Power (W)	Pressure (mbar)	Time (min)
Mo	90	0.2	49	8.7×10^{-3}	10
Cu	90	0.3	8	8.7×10^{-3}	10
In	90	0.3	12	8.7×10^{-3}	10
CuInGa	90	0.4	22	8.7×10^{-3}	10

To improve the parameters, several experiments were done in order to calibrate the sputtering process, which can be found in section 4 and 5.

3.1.4. Quartz crystal microbalance

In-situ thickness measurement was performed using the STM-2XM rate and thickness monitor. This quartz crystal microbalance measures the change in frequency of a quartz crystal resonator, thus, when mass is added to the quartz crystal, the frequency of the resonances changes. The monitor uses the density of this added material to convert the mass information into thickness. Since the flow of material from a deposition is not uniform, it is necessary to calculate the Tooling

Factor (%), which accounts for the different amount of material deposited onto the sensor compared to the substrate.

$$Tooling\ Factor\ (\%) = TF_i \left(\frac{T_m}{T_x} \right) \ ,$$

where TF_i is the initial tooling factor of 100%, T_m is the actual film thickness at the substrate and T_x is the thickness reading of the quartz crystal balance.

3.2. Experimental Procedures

3.2.1. Substrate cleaning and preparation

Prior to any deposition, the substrate must be cleaned with detergent, deionized water and ultrasonic equipment. The substrates are placed in a metal holder and secured with metal bars so that the substrate does not slip.

In total, six baths are performed. The first bath is carried out with deionized water at room temperature and detergent for 10 minutes. The second is performed with water at 60 °C and detergent for 10 minutes. From the third to the sixth bath, the water remains at 60 °C, lasting 10 minutes each. After each bath the deionized water had to be changed and the substrate washed, also with deionized water. After the cleaning procedure, each substrate was blow-dried using a nitrogen gun.

When required, lines were drawn with a permanent marker on the surface of the substrate, which were removed after the deposition to allow a thickness measurement. The substrate was placed in a holder and inserted into a cassette and then introduced into the vacuum chamber (Loading chamber).

The process used the remove the lines after the deposition is called lift off and consists in a bath using acetone and ultrasonic. After the lift off, the sample was blow dried with a nitrogen gun and stored in a sample box.

The samples were named according to the layer deposited on the substrate. Therefore, M for molybdenum, CIG for copper-indium-gallium, CIGS for copper-indium-gallium-selenium and CuIn for copper-indium.

3.2.2. Mo deposition

A Mo layer was deposited as a back contact by DC magnetron sputtering. The Loading chamber was evacuated by a turbomolecular pump to a base pressure of 10^{-6} mbar. The Mo layer was coated onto glass substrates adopting a bilayer process in which a 100nm thick layer was deposited at a chamber pressure of 8.7×10^{-3} mbar followed by a second layer with thickness of 400 nm at 5.6×10^{-3} mbar, the parameters are shown in Table 3.2.

Table 3.2 – Deposition parameters used for Mo sputtering

Layer	Ar (sccm)	Current (A)	Power (W)	Pressure (mbar)	Time (min)
(1) 100 nm	90	0.2	50	8.7×10^{-3}	10
(2) 400 nm	45	0.2	54	5.6×10^{-3}	30

3.3. Characterization

3.3.1. Scanning electron microscopy (SEM)

The scanning electron microscope (SEM) is an instrument that creates magnified images which reveal microscopic-scale information on the size, shape, composition, crystallography and other physical and chemical properties of a specimen [30] by collecting secondary or backscattered electrons created by scanning the sample with a focused electron beam, with energy from 0.1 to 30 keV [31].

SEM's components are shown in Fig. 3.5. The basic operating principle of the SEM involves the emission of electrons by the electron gun into the column, which is equipped with the electron optic elements responsible for focusing the electrons on the sample surface [30]. The interaction of the electron beam and the sample surface produces electron products, such as backscattered electrons, secondary electrons and characteristic X-rays. Therefore, to create images or determine information about samples, different types of detectors can be used.
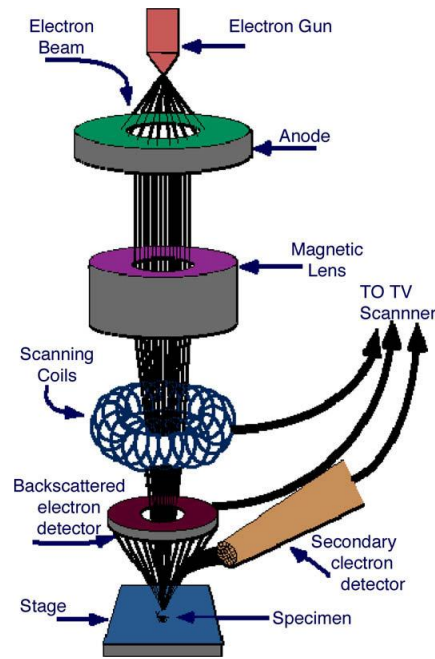
Figure 3.5 - Scanning electron microscope components [31].

Backscattered electrons (BSEs) imaging highlights the spatial distribution of elements or compounds with different atomic number within the top micrometer of the sample. Secondary electron (SE) imaging shows the topography of surface features and is also used for examining thickness variation over topography or thickness in complex multilayers, with thickness higher than 100 nm by the procedure of cross-sectioning [32]. Characteristic X-rays can be used to identify the elemental composition of materials imaged in SEM for all elements with an atomic number greater than boron, since the energy of each X-ray photon is characteristic of the element that produces it [31].

Overall, SEM allows the electron imaging of microstructures, elemental analysis and mapping and electron backscattering for heavy element analysis. However, it has a few limitations since it requires vacuum and the electron beam can damage the sample.

The SEM equipment used in this work was the FEI Quanta 650 FEG (Fig. 3.6).
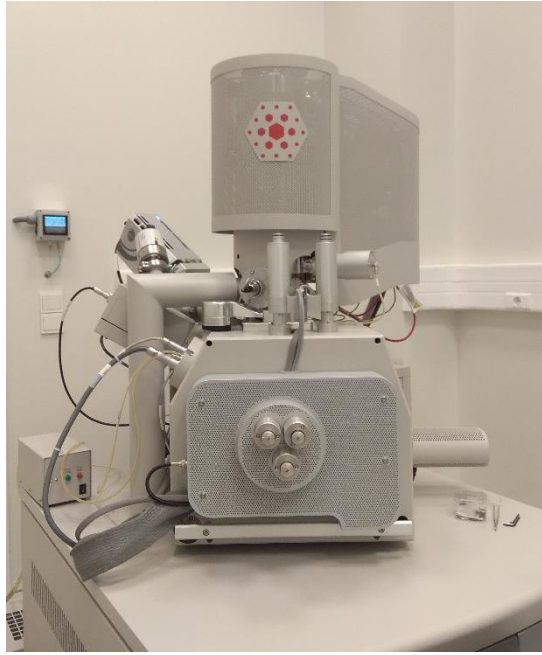
Figure 3.6 - SEM equipment FEI Quanta 650 FEG.

3.3.2. Energy dispersive X-ray spectroscopy (EDX)

The energy dispersive X-ray spectroscopy (EDX or EDS) is a technique used to obtain elemental compositional information of a sample by measuring the energy and intensity distribution of the X-ray signal generated by a focused electron beam. As the electron beam of the SEM is scanned across the sample surface, it generates X-ray fluorescence from the atoms in its path and the energy of each X-ray photon is characteristic of the element that produces it [31]. The software analyzes the X-ray spectrum and assigns the characteristic peaks recognized to specific elements and provides identification of the elements, atomic and weight percent of elements, intensities of the X-rays and other parameters that are electron and elemental atomic number dependent [33]. This technique provides significant information about the chemical composition of thin films allowing stoichiometry adjustments. However, some elements exhibit similar X-ray characteristic peaks making it difficult to identify and quantify the elements, especially if the material is unknown.

3.3.3. X-ray diffraction (XRD)

X-ray Diffraction (XRD) is a powerful technique for analyzing a wide range of materials, which applications include phase analysis, determination of crystalline structure and epitaxial orientation, measurement of thickness and interfacial roughness, determination of texture and residual stress in films [31].

The XRD basic system is composed by an X-ray source, a detector and a sample mount (goniometer). In a simplistic way, the X-rays are produced in an X-ray tube, by electrons striking a copper target. The X-rays exit the tube and are incident on the sample from which they are diffracted into the detector. The beam passes through a slit and a nickel filter that removes $K\beta$ energy before the diffracted beam enters the detector. The results for the XRD are expressed in a graph that plots intensity versus 2-theta.

The XRD equipment used in this work was the X'Pert Pro PANalytical (Fig. 3.7) for phase analysis and determination of crystal structure, using the Bragg Brentano configuration. Between the X-ray source and the detector, is the goniometer, where the sample is placed. When the X-rays from the Cu X-ray tube (X-ray source) are diffracted by the sample, and passes through the receiving slit before being accepted by the detector. The diffraction pattern is measured by collecting information on the angles and intensities of the diffracted X-rays.
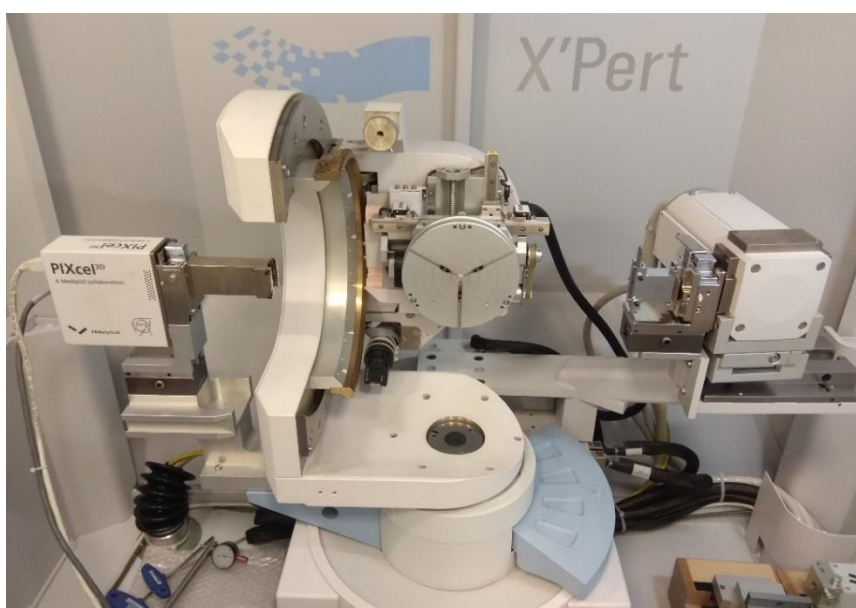
Figure 3.7 – XRD equipment X'Pert Pro PANalytical

Further analysis can be done with the X'Pert Highscore software that allows the selection of specific chemical elements to look for peaks matches with the reference patters from the data base, which gives information about the compound name, structure and phase. The chemical elements inserted to perform the peak match were Cu, In, Ga, Se and Mo (when necessary).

3.3.4. Stylus profilometer

Mechanical profilers, also called profilometers, are instruments used to measure a surface's profile, quantifying the roughness in a surface and height differences between small scale structures [34].

In this instrument a stylus move across the sample while measuring the height variation, therefore, measures the height of a step from the substrate to the film surface. The step is formed by masking during deposition or by masking and etching [35], in this work, the step was formed by lift off, in order to give the height difference between the substrate and the film. Since profilometer is a contact measurement tool, the stylus force can be adjusted to protect the sample's surface from damage. Another complication during the measurement can be the cross contamination between the sample and the stylus.

In this work, the contact profilometer *KLA Tencor Profiler P-16* was used to measure the thickness of films deposited on glass substrate.

4. Calibration of STAR system for Cu(In,Ga)Se$_2$ deposition

Prior to the deposition of CIGS thin films, the STAR system had to be calibrated to control the deposition of the individual materials thickness and film composition. Thickness measurements were performed with a contact profilometer at samples with glass substrate. Surface morphology and composition were determined by scanning electron microscopy (SEM) and energy dispersive X-ray spectrometry (EDX), respectively.

4.1. Cu and In calibration

A series of depositions at different powers were performed using a STAR configuration with two targets, Cu and In, to investigate and optimize the deposition rate and the [Cu]/[In] ratio. Table 4.1 shows the deposition parameters.

Table 4.1 - Deposition parameters used for Cu and In sputtering.

Samples	Ar (sccm)	Cu		In		Pressure (mbar)	Time (min)
		Current (A)	Power (W)	Current (A)	Power (W)		
CuIn 180222 #2	65	0.028	8	0.031	13	6,5x10^{-3}	15
CuIn 180222 #3	65	0.031	9	0.031	13	6,5x10^{-3}	15
CuIn 180222 #4	65	0.048	15	0.052	26	6,5x10^{-3}	15
CuIn 180222 #5	65	0.060	20	0.056	28	6,5x10^{-3}	15

The results of film thickness and chemical composition are shown in Table 4.2. Thickness measurements indicate that a higher power leads to a higher deposition rate, as expected. According to EDX measurements there are small differences in the chemical composition between the samples. The [Cu]/[In] ratio results are in the desired range, which is 0.75 ≤ [Cu]/[III] ≤ 0.95, therefore all films are Cu-poor.

Table 4.2 - Thickness and chemical composition measurement of samples CuIn 180222.

Samples	Thickness (nm)	Deposition Rate (nm/min)	Chemical Composition		
			Cu (at%)	In (at%)	[Cu]/[In]
CuIn 180222 #2	68±11	4.5	45	55	0.84±0.09
CuIn 180222 #3	65±2	4.3	48	52	0.95±0.18
CuIn 180222 #4	230±10	15.3	42	58	0.73±0.14
CuIn 180222 #5	240±40	15.9	44	56	0.80±0.14

Although good results were obtained, it was not possible to continue the depositions using the individual target configuration. The In target presented an extremely unstable behavior, with considerable voltage variation. Therefore, it was not possible to reproduce the depositions. For this reason, this STAR configuration was converted to a single target with Cu, Ga and In ($Cu_{0.5}In_{0.35}Ga_{0.15}$).

4.2. CuInGa calibration

4.2.1. CuInGa Series 1 – Ar flow variation

A series of depositions at different Ar flows (35, 60 and 90 sccm) were performed with a current of 0.03 A for 30 minutes, see Table 4.3. All samples were analyzed by SEM, the results are found in Fig 4.1.

Table 4.3 - Deposition parameters used in the CuInGa Series 1

Sample	Ar (sccm)	Current (A)	Power (W)	Pressure (mbar)	Time (min)
CIG 180629 #1	35	0.03	17	6.2x10-3	30
CIG 180703 #2	60	0.03	16	6.6 x10-3	30
CIG 180703 #3	90	0.03	15	8.7 x10-3	30

SEM images showed a very similar surface for the three samples. All samples presented larger grains and the ones deposited at 60 and 90 sccm presented smaller grains throughout the surface, resulting in a rough surface morphology.
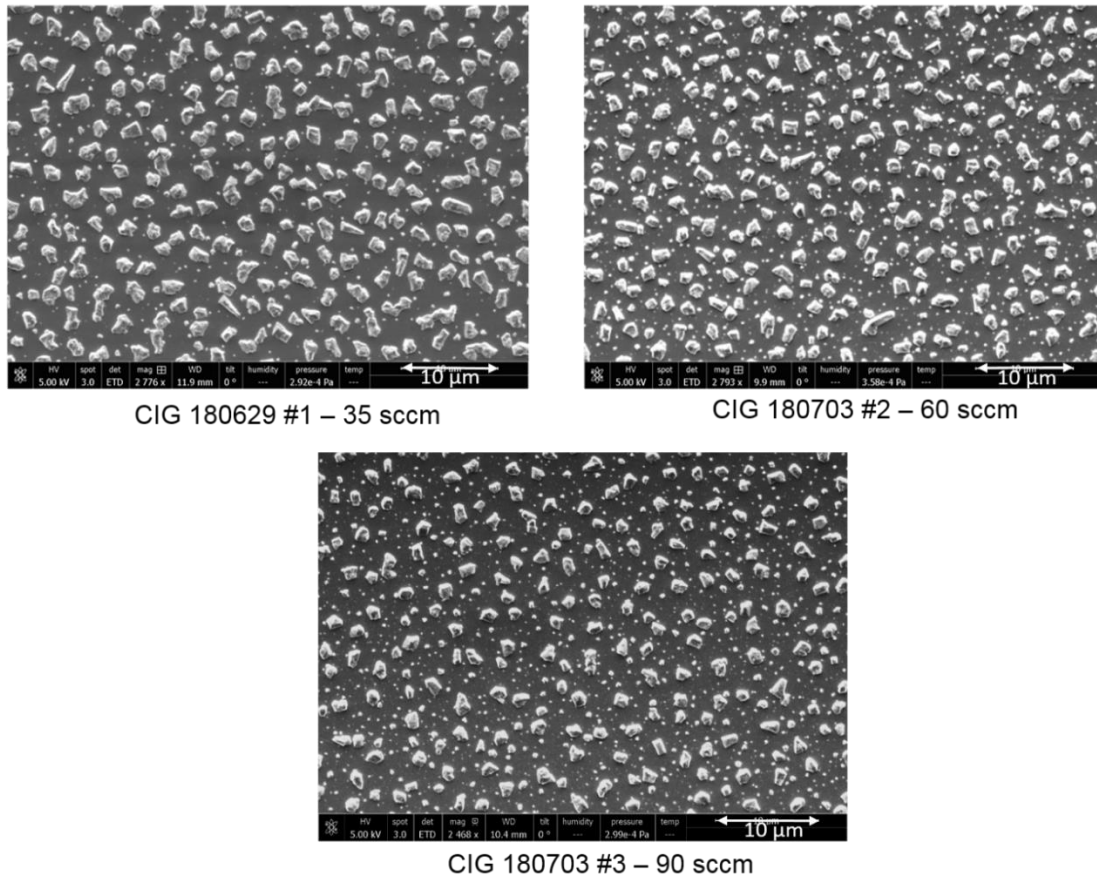
Figure 4.1 – SEM images of CIG film deposited with different Ar flows, 35 (CIG 180629 #1), 60 (CIG 180703 #2) and 90 sccm (CIG 180703 #3). All images were taken with beam voltage of 5 kV.

The thickness of the films was measured by stylus profilometer and chemical composition was evaluated by EDX, see Table 4.4.

Table 4.4 – Thickness and chemical composition measurement of Series 1 samples.

Sample	Ar (sccm)	Thickness (nm)	Deposition rate (nm/min)	Chemical Composition			
				Cu (at%)	In (at%)	Ga (at%)	[Cu]/[III]
CIG 180629 #1	35	340.80 ± 24.82	11	42	42	16	0.72±0.09
CIG 180703 #2	60	262.20 ± 11.81	9	42	42	14	0.75±0.14
CIG 180703 #3	90	236.40 ± 52.93	8	42	44	14	0.72±0.09

The thickness is influenced by the Ar flow, a lower Ar flow leads to a higher deposition rate. When the Ar flow is 35 sccm, the working pressure is 6.2×10^{-3} mbar, which will influence the mean free path of the sputtered atoms and the deposition rate. Therefore, the working pressure should not be to low, reducing the ions and collision, but it should not be too high, causing scattering.

The film composition was also analyzed to determine if the ternary target ($Cu_{0.5}In_{0.35}Ga_{0.15}$) stoichiometry remains after deposition. According to EDX measurements there were small differences in the composition between the samples, but a significant difference to the target composition. However, the [Cu]/[III] ratio indicates a slightly Cu-poor film, as desired. This can be related with the grains present at the film, which according to EDX analysis presented elevated In concentration. Thus, it appears that for CIG deposition at room temperature In-rich segregation on the film surface occurs.

With the analysis it became clear that the chemical composition is similar for all samples and the deposition rate is higher at 35 sccm. However, in the STAR system, with an Ar flow of 35 sccm, the sputtering power is almost at the limit, making it impossible to increase the power and consequently, the deposition rate. Since the deposition rate is influenced by the working pressure and sputtering power, it was necessary to increase the Ar flow in order to lower the voltage, which allowed the increase of the sputtering power and the deposition rate. Hence, Ar flow of 45 sccm was selected for the rest of the work.

4.2.2. CuInGa Series 2 – Power variation

The first deposition was performed with power of 36 W, pressure of 9.8×10^{-3} mbar and Ar flow of 45 sccm (Table 4.5). However, to ignite the magnetron it was necessary to increase the chamber pressure. The second deposition was performed with power of 26 W, pressure of 6.6×10^{-3} mbar and Ar flow of 45 sccm.

Table 4.5 - Deposition parameters used in the CuInGa Series 2

Sample	Substrate	Ar (sccm)	Power (W)	Pressure (mbar)	Time (min)
CIG 180710 #1	Glass	45	36	9.8x10-3	30
MCIG 180710 #1	Glass/Mo				
CIG 180710 #2	Glass	45	26	6.6x10-3	30
MCIG 180710 #2	Glass/Mo				

The results of SEM characterization are shown in Fig. 4.2. SEM images show a very similar surface morphology. The CuInGa precursor layer presents large size In grains, resulting in a rough surface morphology, similar to the images from the Series 1 (Ar flow variation). Therefore, it appears that the power does not significantly affect the film morphology.
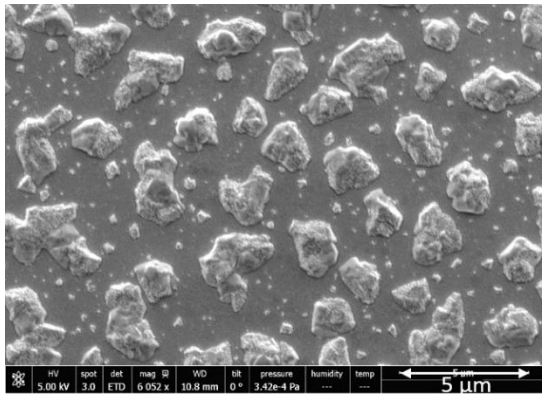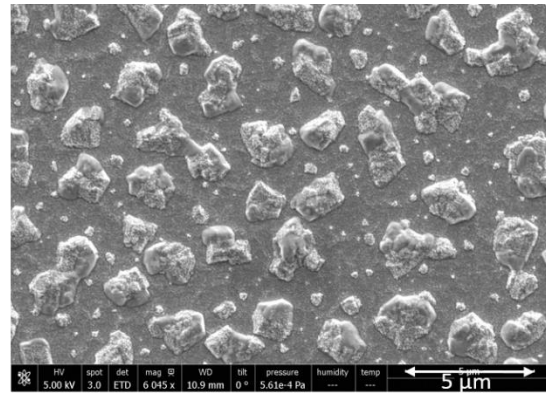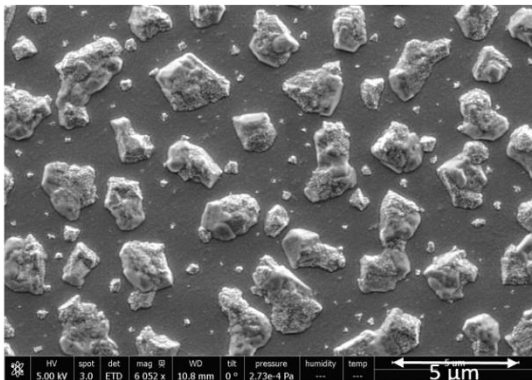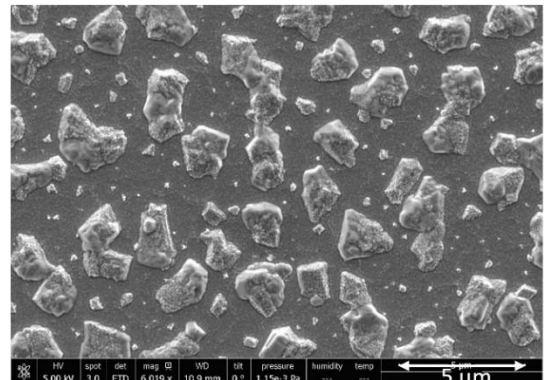
Figure 4.2 – SEM images of CIG film deposited with power of 36 W (CIG and MCIG 180710 #1) and 26 W (CIG and MCIG 180710 #2). All images were taken with beam voltage of 5 kV.

Further characterization was done for thickness and chemical composition (Table 4.6). Thickness measurements were done for samples CIG 180710 #1 and #2 by stylus profilometer and as expected, the power influences the thickness, a higher power leads to a higher deposition rate. In terms of composition, all samples presented similar values. The [Cu]/[III] ratio indicates a slightly Cu-rich film in three samples and this can be explained by a different approach used during the EDX measurements, where the grains were avoided in the selected measurement area.

Table 4.6 – Thickness and chemical composition measurement values of Series 2 samples.

Sample	Power (W)	Thickness (nm)	Deposition rate (nm/min)	Chemical Composition			
				Cu (at%)	In (at%)	Ga (at%)	[Cu]/([In]+[Ga])
CIG 180710 #1	36	441.20 ± 28.96	14.7	50	33	16	1.02±0.12
MCIG 180710 #1				54	29	17	1.17±0.15
CIG 180710 #2	26	397.04 ± 5.33	13.2	50	32	18	1.02±0.10
MCIG 180710 #2				49	31	20	0.96±0.04

Next depositions were done with power of 26 W. Although this sample presented a lower deposition rate, it was not necessary to change the pressure to start the process.

4.3. Selenium

For a complete calibration of the Se source, three calibrations were required: (1) Se cracker temperature (2) tooling factor and (3) deposition rate.

(1) Se cracker temperature calibration

The Se source is controlled by the STAR software, where the Se cell temperature (T_{Se}) and Se cracker temperature (T_{Cr}) are entered into the program. In the STAR software, the T_{Cr} is given in percentage (%), which corresponds to an applied power and temperature. Therefore, a measurement with a pyrometer was carried out to have quantitative information about the Se cracker temperature (T_{Cr}). Figure 4.3 shows the power applied and the temperature variation as a function of the Se cracker temperature (%) with the Se cell temperature (T_{Se}) fixed at 300 °C.
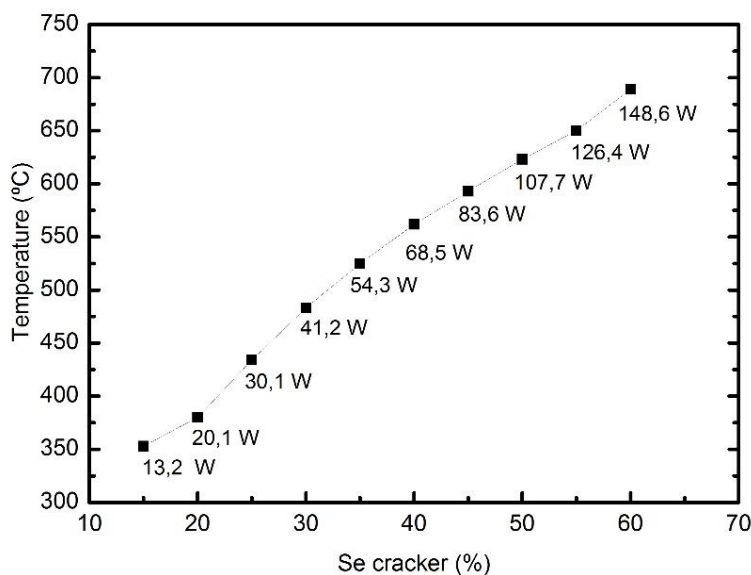
Figure 4.3 – Correlation between temperature variation as a function of the Se cracker (%) and the power applied to the Se cracker.

The temperature varies from 350 °C to 689 °C as the power applied to the Se cracker increases from 13 W (15%) to 149 W (60%). In the following, Se depositions were done with the Se cracker at 45%, which correspond to a power of 84 W and temperature of approximately 595 °C.

(2) Tooling factor

The second calibration was performed to evaluate the tooling factor (see section 3.3). A deposition with T_{Se} = 300°C, T_{Cr} = 595 °C and V_{Se} = 9.4 mm were carried out for 20 min while monitoring with a quartz crystal microbalance and simultaneously depositing on an unheated glass substrate.

The thickness and deposition rate given by the monitor during deposition was 2.86 kÅ and 2.1 Å/s, respectively. However, a thickness measurement was performed at the sample by cross-section at SEM and the average thickness was 2.57 μm. Thus, the Tooling Factor was calculated to 898%, which was entered into the program.

(3) Deposition rate

After established the tooling factor the last calibration was carried out to determine the deposition rate as a function of the Se valve opening, see Figure 4.4.
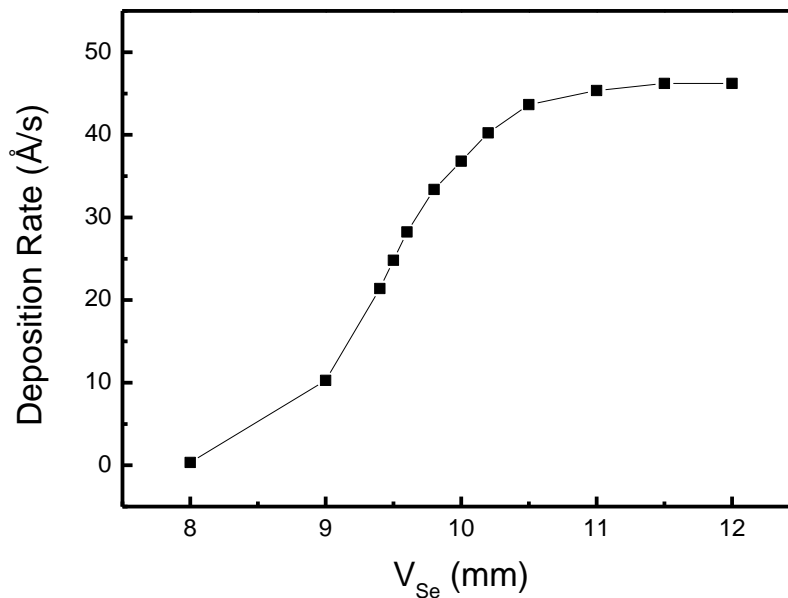
Figure 4.4 – Correlation between the deposition rate as a function of the Se valve opening.

The deposition rate was measured with the thickness monitor according to the V_{Se} variation. It was verified that V_{Se} = 8 mm presented a deposition rate of 0.3 Å/s, which is the minimal flow possible. Amid 9 and 10 mm the deposition rate varies from 10.3 to 36.8 Å/s, respectively. From 11.5 mm the deposition rate was constant, with 46.2 Å/s, indicating that the valve is completely open. Thus,

the valve setting allows the Se flow control. However, other parameters, such as Ar flow, might also influence the deposition rate.

5. Deposition of Cu(In,Ga)Se$_2$ thin film results

In this work three deposition processes for Cu(In,Ga)Se$_2$ (CIGS) were tested: (1) co-deposition of Cu, In, Ga and Se, where Cu, In and Ga are sputtered and Se is evaporated at the same time, (2) Cu, In, Ga deposition by sputtering with a post-selenization and (3) a pulsed deposition of Cu, In, Ga by sputtering and Se by evaporation. Surface morphology, thickness, composition, phase and structure were determined by scanning electron microscopy (SEM), cross-section at SEM, energy dispersive X-ray spectrometry (EDX) and X-ray diffraction (XRD), respectively.

5.1. Cu(In,Ga)Se$_2$ substrate temperature calibration

In the first set a CIGS co-deposition was performed in two samples simultaneously, CIGS 180717 and MCIGS 180717 #3 for 30 minutes. The CuInGa sputtering was performed with a power of 26 W and Ar flow of 45 sccm (Table 5.1) and the Se source parameters were T_{Se} = 300 °C, T_{Cr} = 45%, V_{Se} = 12 mm. The desired substrate temperature (T_{sub}) of 500 °C was entered into the STAR software. Once the sample was removed from the chamber, it was observed that it had a slight glass deformation, although sample CIGS 180717 did not show any deformation. The glass bending could result from two efects: (i) the presence of the Mo layer may have increased the sample temperature due to the absorption of infrared radiation in the Mo layer, and/or (ii) some stress between the Mo layer and the glass might occur due to different thermal expansion coefficienct of the two materials. It is also important to highlight that the substrate temperature is nominal, thus, the actual temperature might be up to 70°C higher.

In order to verify the temperature influence, a substrate with Mo layer was heated up to 570 °C. In Figure 5.1 it is possible to visualize the sample deformation after heating. To avoid this problem, the depositions were done at 450 °C.

Figure 5.1 - Sample (glass/Mo) after heating at 570°C.

The second deposition was performed simultaneously in two samples, CIGS 180726 (SLG) and MCIGS 180726 #2 (SLG + Mo) for 54 min. The CuInGa sputtering was performed with a power of 28 W and Ar flow of 45 sccm (Table 5.1), Se source parameters were T_{Se} = 300 $^{\circ}$C, T_{Cr} = 45%, V_{Se} = 12 mm, and T_{sub} = 450 $^{\circ}$C.

Table 5.1 – Deposition parameters used in the CIGS substrate temperature calibration.

Sample	Ar (sccm)	Power (W)	Tsub (ºC)	Time (min)
MCIGS 180717 #3	45	26	500	30
MCIGS 180726 #2	45	28	450	54
CIGS 180726	45			

SEM images (Fig 5.2) show a significant morphology difference between the samples. Sample MCIG 180717 #3 presented a rough surface with a grain size of 1 – 2 µm, which is also noticeable at the cross-sectional image. Sample MCIGS 180726 #2 images presented a very homogeneous surface.
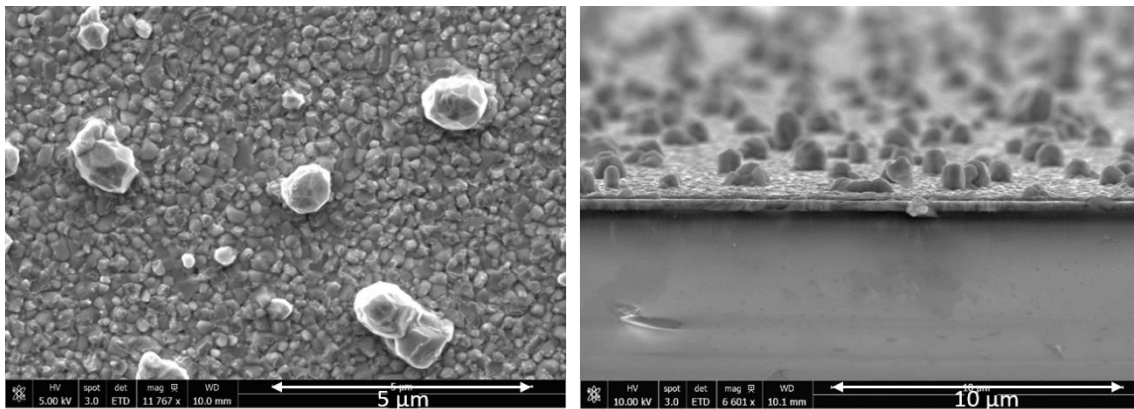
MCIGS 180717 #3
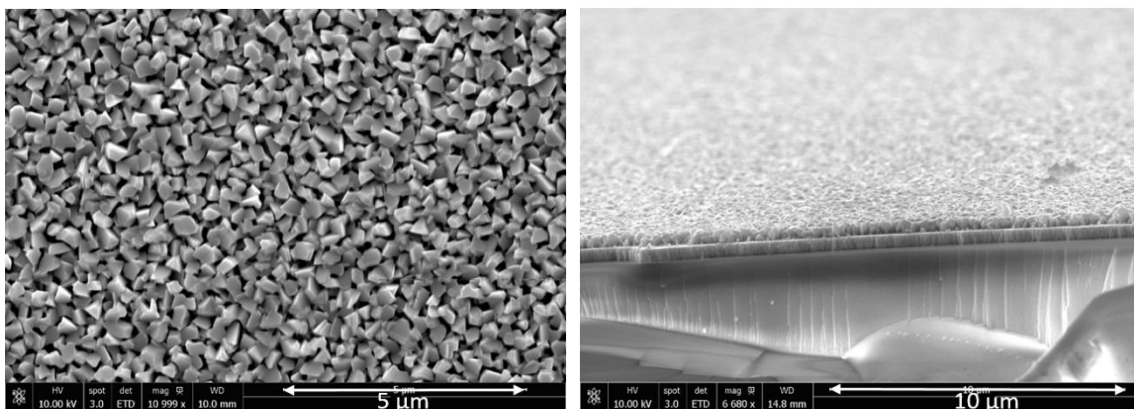
MCIGS 180726 #2

Figure 5.2 – Surface and cross-sectional SEM images of samples MCIGS 180717 #3 (top) and MCIGS 180726 #2 (bottom). Surface image of sample MCIGS 180717 #3 was obtained using a beam voltage of 5 kV and 10 kV for the other samples.

Thickness was measured by cross-section at SEM and film composition by EDX, see Table 5.2. Sample MCIGS 180717 #3 presented a higher Cu concentration, which is confirmed by the [Cu]/[III] ratio. This can be related to the grains present in the film that according to EDX analysis, are Cu-rich. Sample MCIGS 180726 #2 presented higher concentration of Se than expected (50 at%). Therefore, in this case, the film surface morphology and chemical composition seems to be significantly influenced by the T_{sub}. Thus, due to the lower T_{sub}, more Se remains on the surface, and less re-evaporates.

Table 5.2 - Thickness and chemical composition measurement values of CIGS temperature substrate calibration.

Sample	Thickness (nm)	Chemical Composition				
		Cu (at%)	In (at%)	Ga (at%)	Se (at%)	[Cu]/[III]
MCIGS 180717 #3	281 ± 37	33	15	12	40	1.22±0.09
MCIGS 180726 #2	448 ± 8	11	14	3	72	0.64±0.12

5.2. Cu(In,Ga)Se$_2$ co-deposition

The co-deposition, or reactive sputtering consists in adding a reactive gas to the sputtering process in order to produce a compound thin film. With this method, it is possible to deposit CIGS thin films using a one-step process. A triple substrate holder was used to enable the deposition in three samples simultaneously, when needed.

The process pressure, substrate temperature and duration were 6.6×10^{-3} mbar, 450 $^{\circ}$C and 160 minutes, respectively. The CIG target was sputtered at a power of 26 W and Ar flow of 45 sccm (Table 5.3), the Se source parameters were T_{Se} = 300 $^{\circ}$C, T_{Cr} = 45%, V_{Se} = 10mm, and T_{sub} = 450 $^{\circ}$C. During the deposition, the magnetron stopped a few times and it was notice that this happened when the voltage reached a certain value. In order to prevent this, it was decided to keep the power at maximum during the next deposition.

A second deposition was performed at a process pressure, substrate temperature and duration of 6.6×10^{-3} mbar, 470 $^{\circ}$C and 150 minutes, respectively. During the deposition process, the average power was 29 W and Ar flow of 45 sccm (Table 5.3), the Se source parameters were T_{Se} = 300 $^{\circ}$C, T_{Cr} = 45%, V_{Se} = 9.5 mm, and T_{Sub} = 470 $^{\circ}$C.

Table 5.3 – Deposition parameters used in CIGS co-deposition.

Sample	Ar (sccm)	Power (W)	Tsub ($^{\circ}$C)	Time (min)
MCIGS 180813 #2	45	26	450	160
MCIGS 180824 #1	45	29	470	150

CIGS thin films were characterized by SEM to obtain surface images (Fig. 5.3). Both samples presented a practically identical surface, with no significant difference.
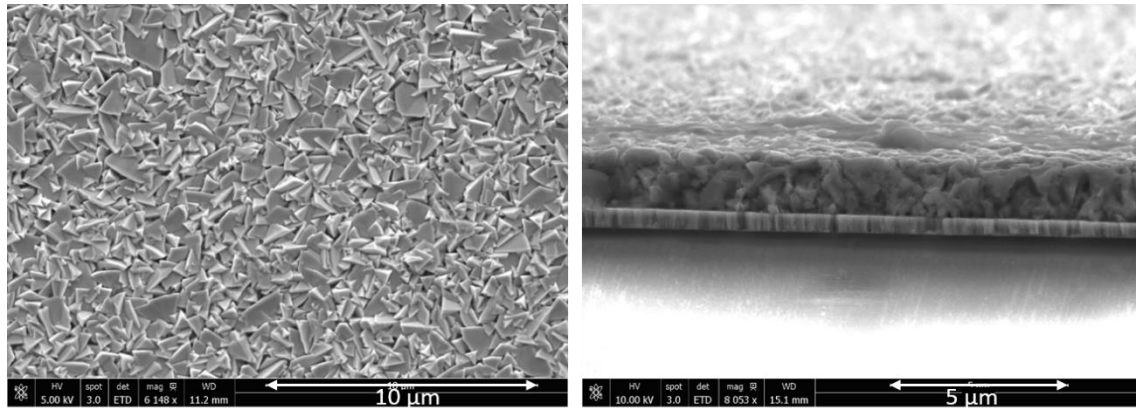
MCIGS 180813 #2
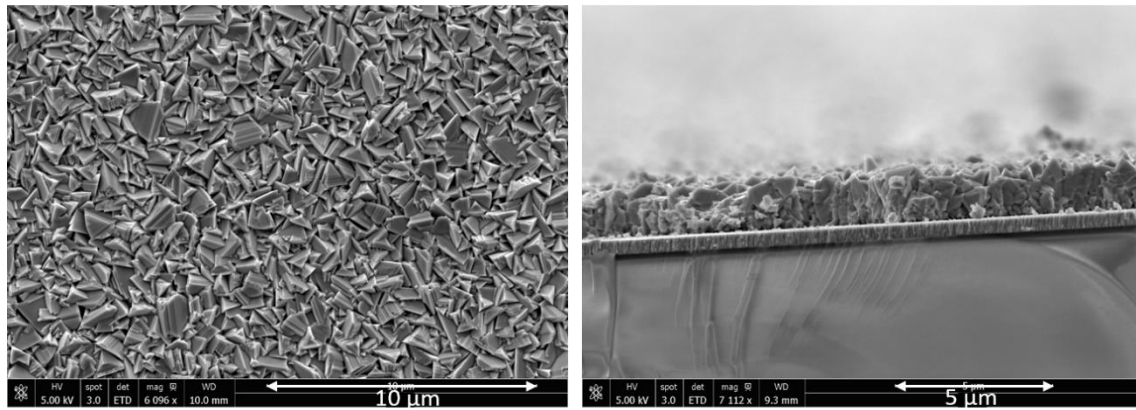
MCIGS 180824 #1

Figure 5.3 - Surface and cross-sectional SEM images of samples MCIGS 180813 #2 (top) and MCIGS 180824 (bottom). Cross-sectional images of sample MCIGS 180717 #3 was obtained using a beam voltage of 10 kV and 5 kV for the other samples.

Thickness measurements are consistent for both samples (Table 5.4), considering that the sample MCIGS 180824 #1 was deposited with a higher power, less duration and uninterrupted. The compositions were also similar, however with the Se addition, the expected chemical composition should be 25, 17.5, 7.5 and 50 at% Cu, In, Ga and Se, respectively. Thus, both samples show an In concentration higher than expected for the target stoichiometry. The [Cu]/[III] ratio values are slightly Cu-poor, as desired ($0.75 \leq$ [Cu]/[III] ≤ 0.95).

Table 5.4 - Thickness and chemical composition measurement values of CIGS co-deposition samples.

Sample	Thickness (nm)	Deposition Rate (nm/min)	Chemical Composition				
			Cu (at%)	In (at%)	Ga (at%)	Se (at%)	[Cu]/[III]
MCIGS 180813 #2	1667±195	10.42	24	20	7	50	0.90±0.05
MCIGS 180824 #1	1747±224	11.65	22	21	7	50	0.81±0.04

XRD measurements were carried out in the Bragg-Brentano configuration and the respective analysis was performed with the software *Highscore*, as mentioned in section 3.3.3. The elements

introduced in the software were Cu, In, Ga, Se and Mo. Figure 5.4 present the XRD measurement along with the respective peak and Miller indices, which corresponds to different crystalline planes.

Both samples presented tetragonal CIGS structure and different peaks were identified, where the predominant peaks are for (112), (220) and (312) planes, thereof are positioned, at $2\theta =26.8°$, 44.5° and 52.8° for sample MCIGS 180813 #2, and at the same values ±1 for sample MCIGS 180824 #1. A single peak for Mo positioned at 40.6° and 40.4° were identified, which corresponds to (110) plane in a cubic structure for samples MCIGS 180813 #2 and MCIGS 180824 #1, respectively. These CIGS and Mo planes and positions are consistent with the literature [29] [36] [37] [38]. The presence of unidentified peaks occurs due to the selection of specific chemical elements (Cu, In, Ga, Se and Mo) for the pattern analysis in the *Highscore* software (see Section 3.3.3)
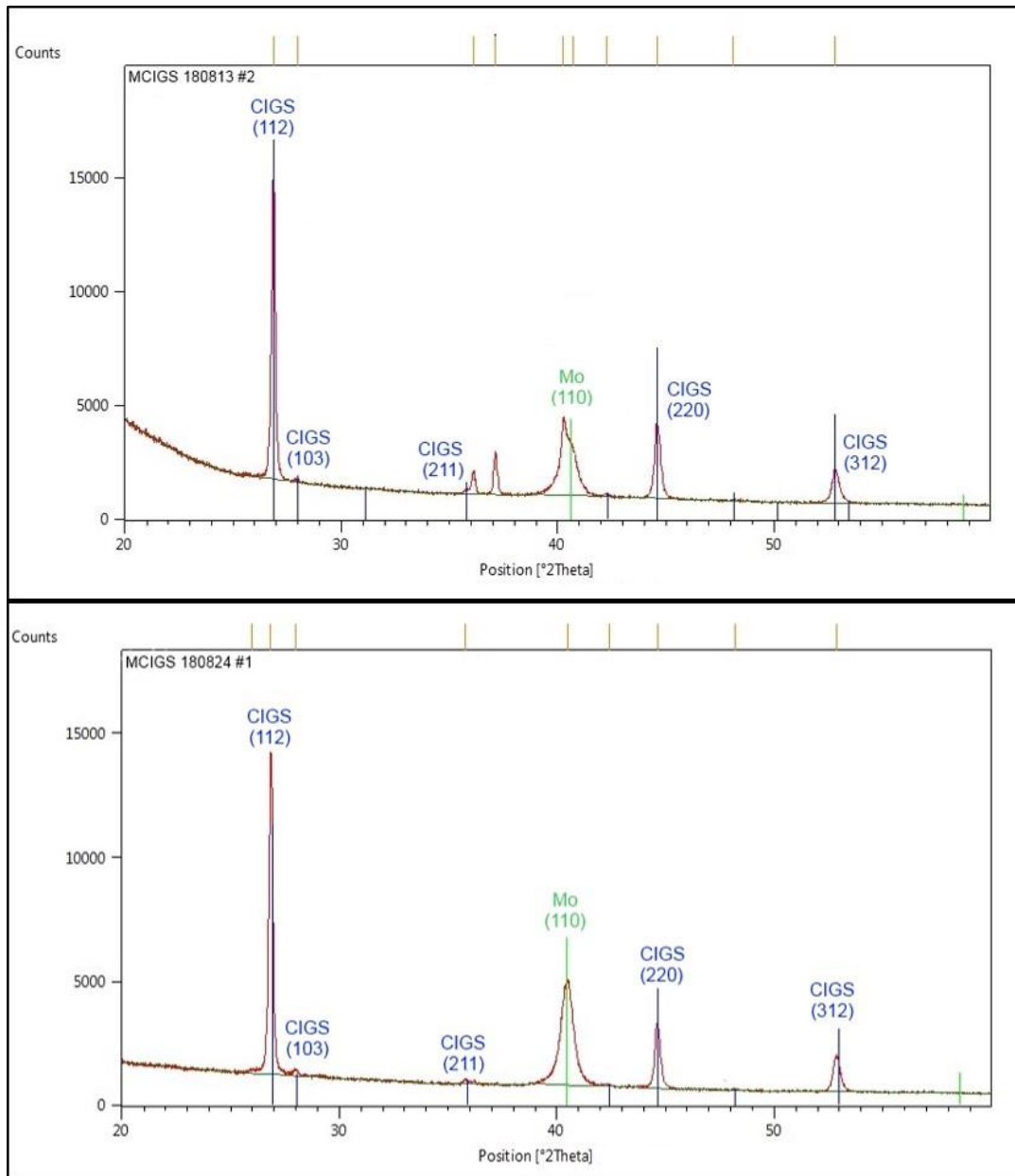
Figure 5.4 - XRD spectra in Bragg Brentano configuration of CIGS films co-deposited on SLG/Mo substrates. Vertical lines correspond to the matching peaks found by software Highscore, where CIGS is blue and Mo is green

5.3. CIG sputtering with post-selenization

In this method a two-stage process is performed where a CuInGa deposition by sputtering is followed by a post-selenization.

The sputtering process pressure and duration were 6.6×10^{-3} mbar and 150 minutes, respectively. The CIG target was sputtered at a power of 29 W and Ar flow of 45 sccm. After the sputtering process, the sample remains inside the chamber and the Se valve is kept open during this final process. The Se source parameters for the post-selenization were $T_{Se} = 300$ $^{\circ}$C, $T_{Cr} = 45\%$, $V_{Se} = 10$mm, with $T_{sub} = 450$ $^{\circ}$C. The samples were selenized in a pressure of 7.8×10^{-7} mbar for 20 minutes. Since the post-selenization occurs after the sputtering, there is no flow of Ar inside the chamber, therefore the process has a working pressure of 10^{-7} mbar.

The SEM images (Fig 5.5) of the precursor CIG thin film (MCIG 180817) presented a homogeneous topography, with similar grain sizes throughout the surface. Samples MCIG 180817 #PS1 and #PS2, presented a similar uneven topography.
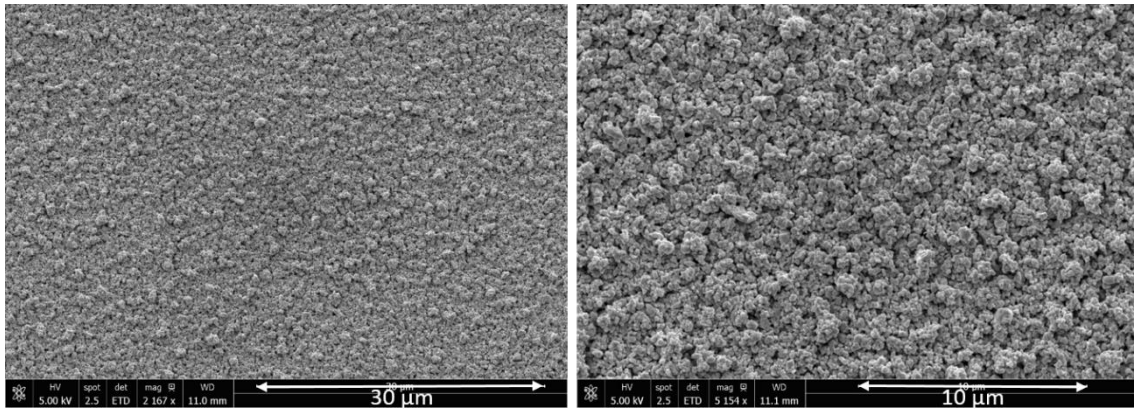
MCIG 180817
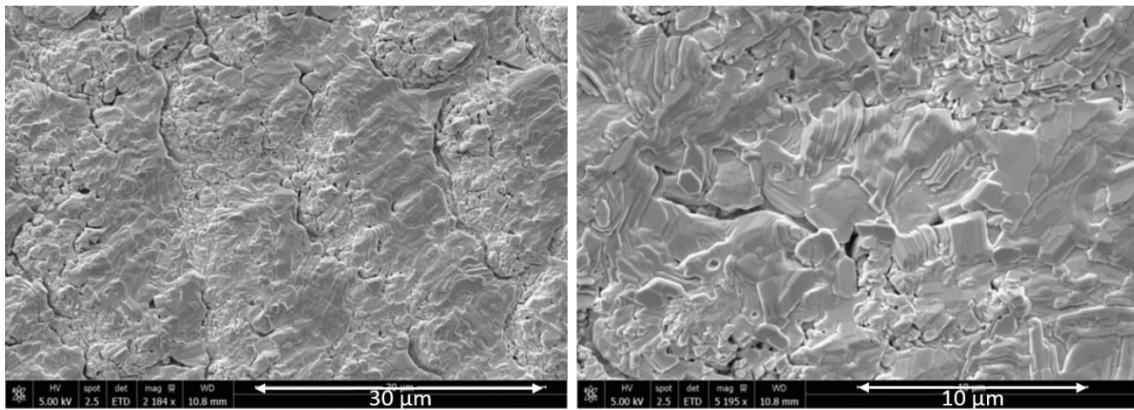
MCIG 180817 #PS1
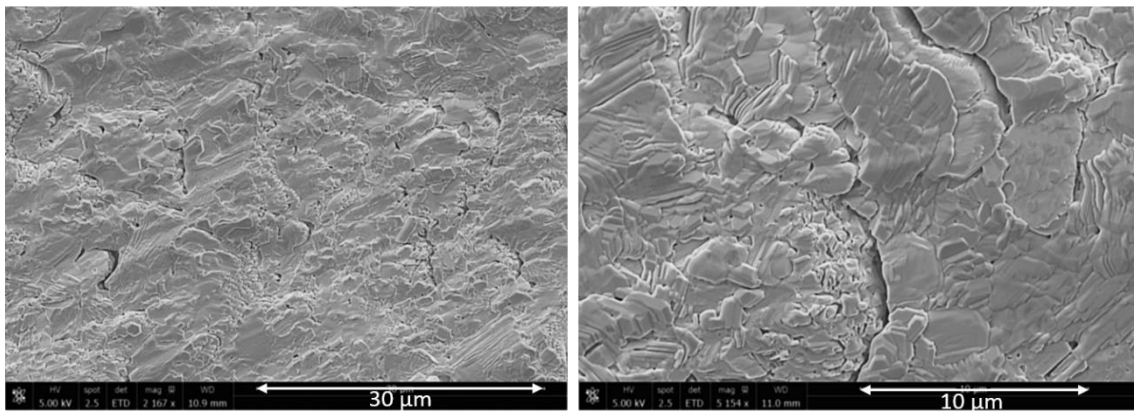
MCIG 180817 #PS2

Figure 5.5 - Surface images of CIG thin films before (MCIG 180817) and after (MCIG 180817 #PS1 and #PS 2) the selenization. All images were obtained with beam voltage of 5 kV.

Table 5.5 displays the thickness and chemical composition results. In this case, thickness measurements by cross-section (Fig. 5.6) were performed at sample MCIG 180817 and MCIG 180817 #PS1, in order to verify the thickness prior and after selenization. A difference of 952.05 nm was observed between the samples, therefore the post-selenization process increased the film thickness in almost 1 µm. Since samples MCIG 180817 #PS1 and #PS2 were deposited at the same time, the thickness was measured in only one sample.

| MCIG 180817 | MCIG 180817 #PS1 |

Figure 5.6 - Cross sectional images of samples before (MCIG 180817) and after (MCIG 180817 #PS1) the selenization. All samples were obtained with beam voltage of 10 kV.

According to EDX measurements all samples presented composition values different from the target stoichiometry. Sample MCIG 180817 presented a higher In concentration than expected, however the [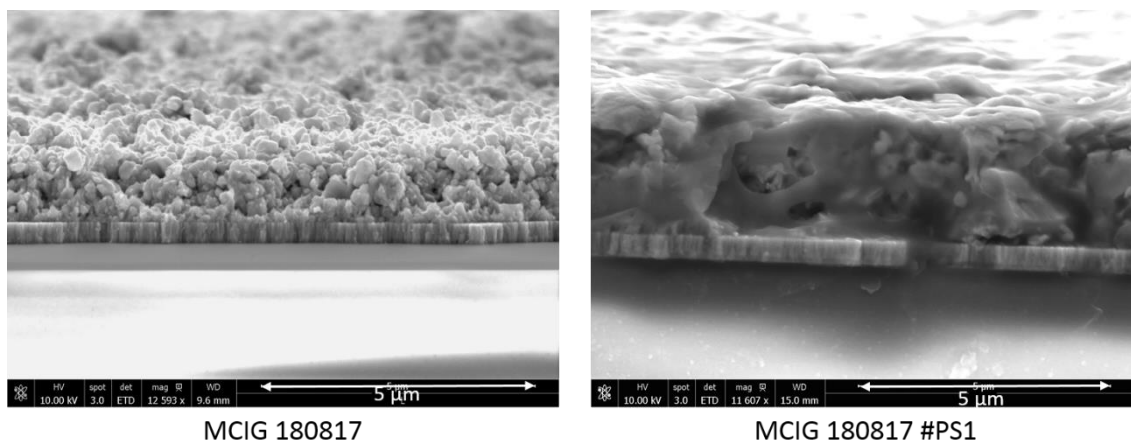Cu]/[III] ratio gave a value of 0.74, which is within the desired range. Samples MCIG 180817 #PS1 and #PS2 had very similar composition values, since both samples were sputtered and selenized simultaneously. The individual concentration and the [Cu]/[III] ratio indicate that after the selenization both samples are Cu-rich.

Table 5.5 - Thickness and chemical composition measurement values of CIG with post-selenization samples.

Sample	Thickness (nm)	Chemical Composition				
		Cu (at%)	In (at%)	Ga (at%)	Se (at%)	[Cu]/[III]
MCIG 180817	1562±211	42	43	14	-	0.74±0.04
MCIG 180817 #PS1	2514±251	31	15	4	50	1.6±0.11
MCIG 180817 #PS2		32	14	4	49	1.8±0.09

Figure 5.7 shows XRD patters of the samples prior (MCIG 180817) and after the selenization (MCIG 180817 #PS1 and #PS2). The characteristic peak (110) from cubic Mo are present in all samples. XRD results indicated that sample MCIG 180817 consist of pure In and Cu. Three intense peaks related to In are observed at 32.9°, 36.3° and 39.0°, which represent (101), (002) and (110) planes in a cubic structure. A single peak for Cu positioned at 42.8° were identified, which corresponds to (111) plane in a cubic structure.

As expected, the samples with post selenization presented similar XRD results. Both samples presented tetragonal CIGS structure, where the predominant peaks are (112), (220) and (312),

thereof are positioned at 26.8°, 44.5°, 52.7° for sample #PS1, and at the same values ±1 for sample #PS2. Characteristic peaks from hexagonal CuSe and tetragonal $CuInSe_2$ are also present in both samples. Therefore, the presence of CuSe in the XRD and EDX results confirm a Cu-rich film. The presence of unidentified peaks occurs due to the selection of specific chemical elements (Cu, In, Ga, Se and Mo) for the pattern analysis in the *Highscore* software (see Section 3.3.3)
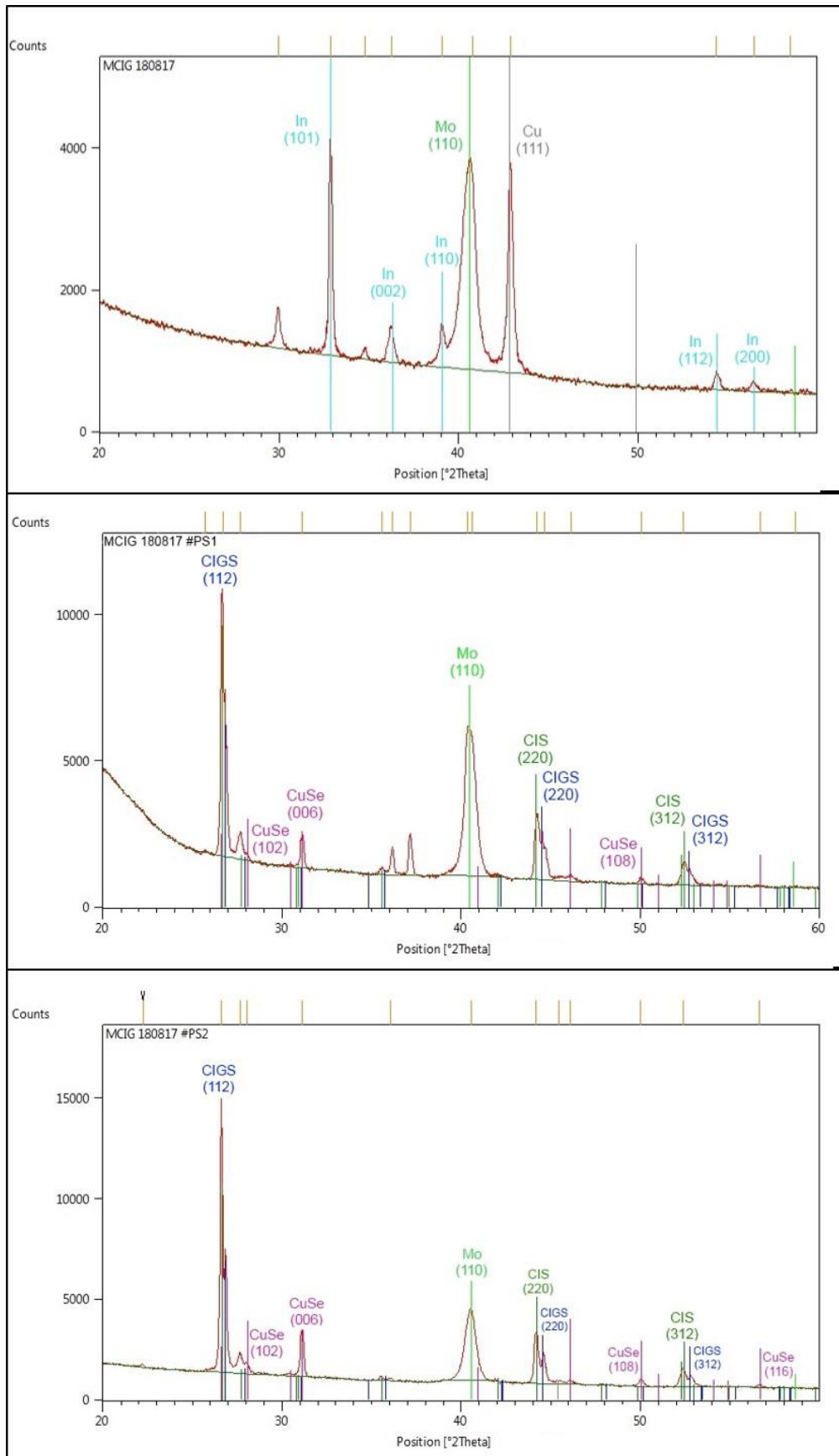
Figure 5.7 - XRD spectra in Bragg Brentano configuration of CIGS films deposited by CIG sputtering followed by post-selenization on SLG/Mo substrates. Vertical lines correspond to the matching peaks found by software Highscore, where CIGS is blue, Mo is green, CuSe is pink and CuInSe₂ is dark green.

5.4. CIGS pulsed deposition

For the pulsed deposition, a recipe was created in order to allow the deposition with the desired parameters. In this process, the CuInGa target was sputtered intercalating a low and high current along the V_{Se} closing and opening. Therefore, while the Se valve was closed, a high current of 60 mA was used during 5 seconds and when the Se valve was open, a low current of 20 mA was used for 2 seconds (Fig 5.8). This cycle was repeated 1400 times. The Se source parameters for this deposition were T_{Se} = 300 ^{o}C, T_{Cr} = 45%, V_{Se} = 10mm, with T_{sub} = 450 ^{o}C. The process pressure and duration were $6.6x10^{-3}$ mbar and 161 minutes, respectively.
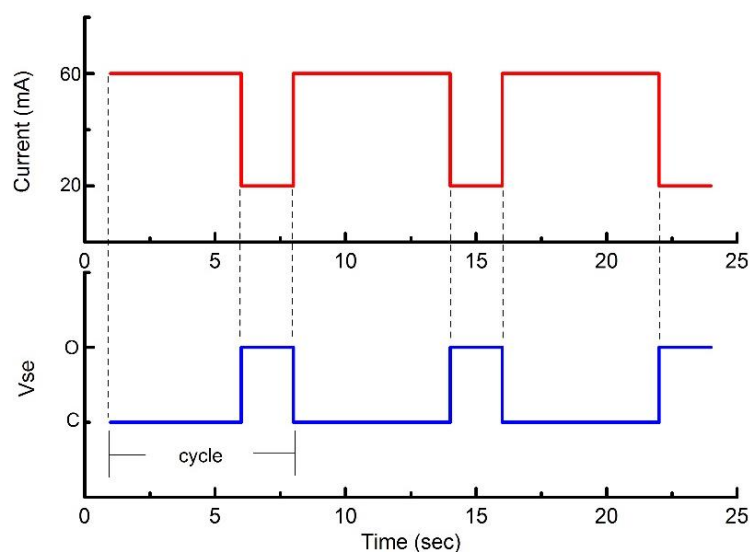
Figure 5.8 - Schematic of the cycle during the pulsed deposition. One cycle corresponds to 5 sec of high current (60 mA) with the V_{Se} closed and 2 sec of low current (20 mA) with the V_{Se} open.

The SEM images (Fig. 5.9) show significant differences in the sample surface morphology. Although the two samples show an uneven topography, sample PCIGS 180905 surface is similar to those found in the post-selenization process, while sample MPCIGS 180905 presented islands throughout the film, resulting in a rough surface morphology. Considering that both samples were deposited simultaneously, the Mo layers seems to portray a significant function in the surface morphology. From SEM and cross-sectional images (Fig 5.10) it is possible to identify some voids in the film, this may be related to the loss of Se during and after the deposition.
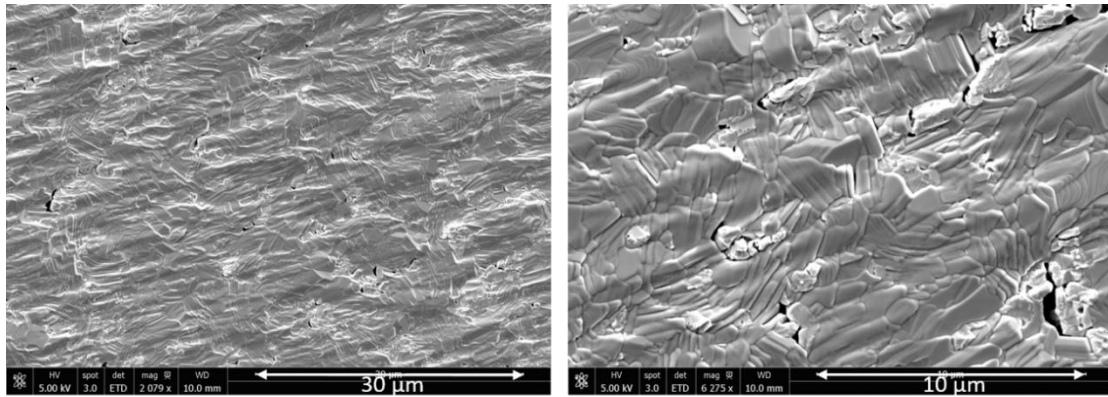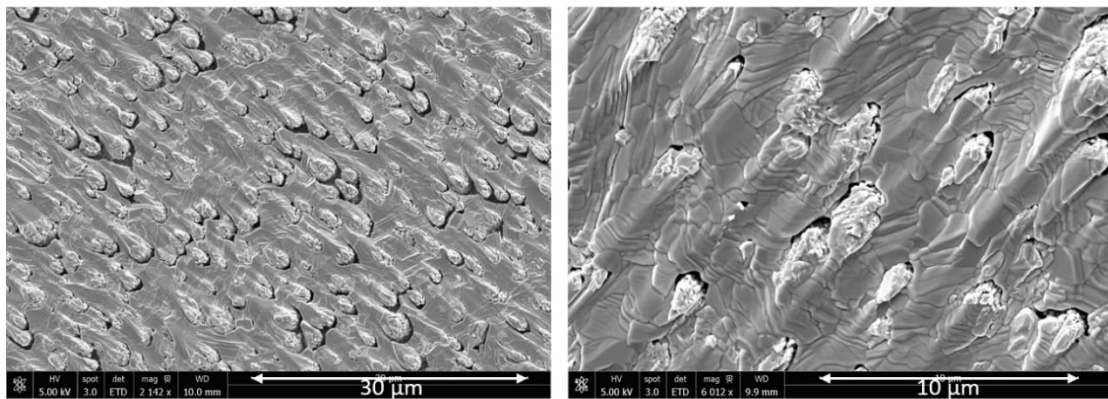
Figure 5.9 – Surface images of samples PCIGS 180905 and MCIGS 180905. All images were obtained with beam voltage of 5 kV.

Figure 5.10 – Cross-sectional SEM images of samples PCIGS 180905 and MPCIGS 180905. All images were obtained with beam voltage of 5 kV.

Thickness and chemical composition measurements (Table 5.6) are consistent for both samples. EDX analysis of chemical composition indicates a Cu-rich film in both samples, which is confirmed by a [Cu]/[III] ratio of 2.3 and 2.2 for samples PCIS 180905 and MPCIGS 180905, respectively.

Sample	Substrate	Thickness (nm)	Chemical Composition				
			Cu (at%)	In (at%)	Ga (at%)	Se (at%)	[Cu]/[III]
PCIGS 180905	Glass	2108.88±232	34	8	7	51	2.3±0.22
MPCIGS 180905	Glass/Mo	2230.42±194	33	9	6	51	2.2±0.08

According to XRD analysis (Fig. 5.11) characteristic peaks from tetragonal CIGS and hexagonal CuSe are present in both samples. Different peaks corresponding to CIGS compound were identified, which are (112), (220) and (312), thereof are positioned at 26.9°, 44.6° and 52.8° for sample PCIGS 180905, and at the same values ±1 for sample MPCIGS 180905. Different peaks for CuSe were identified, which are (102), (103), (006), (107), (110), (108), (116), thereof are positioned at 28.1°, 30.4°, 31.1°, 45.4°, 46.0°, 49.9° and 56.6°, respectively. The presence of CuSe in the film also indicates a Cu-rich film, which is consistent with the EDX results.
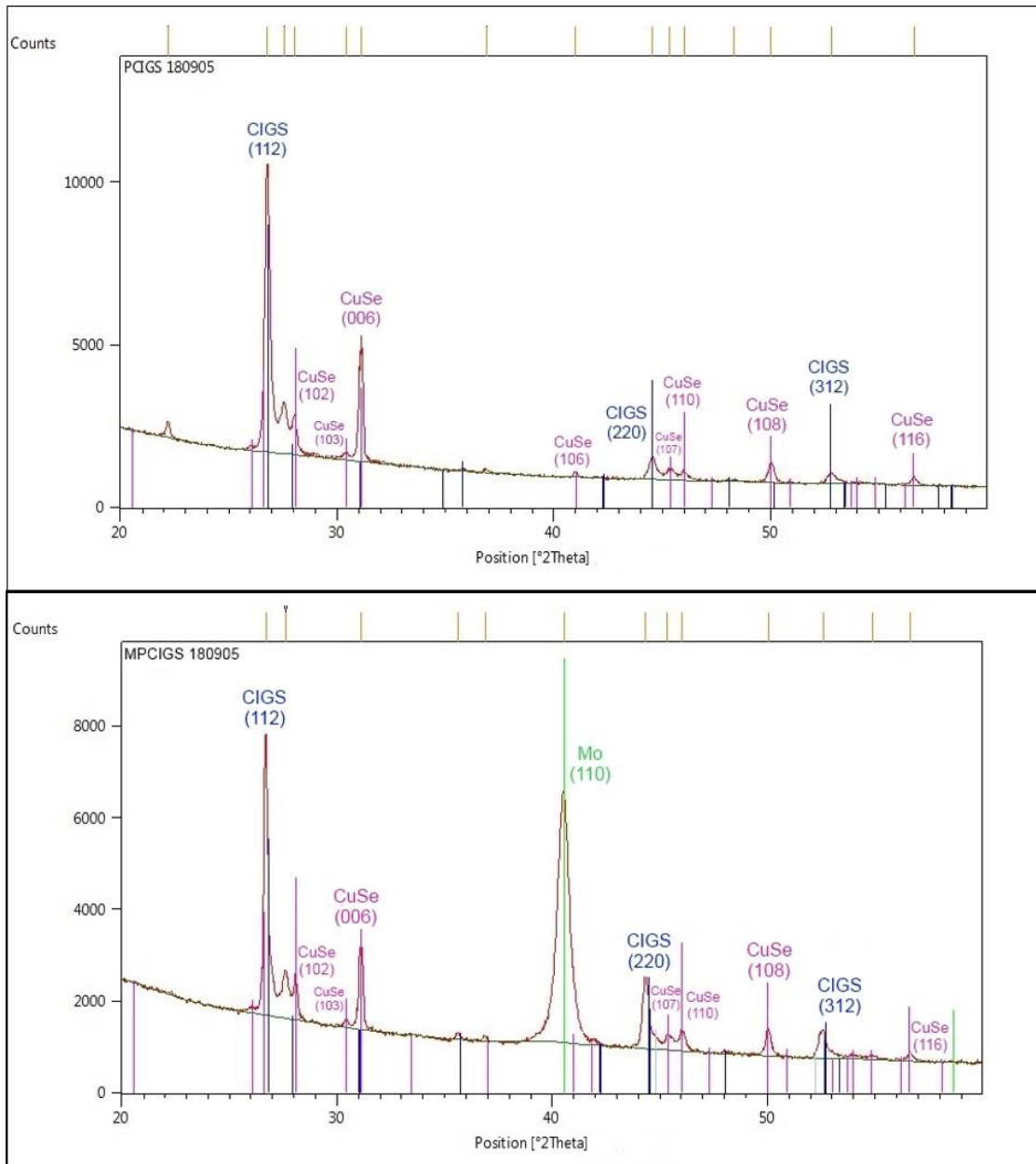
Figure 5.11 - XRD spectra in Bragg Brentano configuration of CIGS films deposited by pulsed deposition on SLG (PCIGS 180905) and SLG/Mo (MPCIGS 180905) substrates. Vertical lines correspond to the matching peaks found by software Highscore, where CIGS is blue, Mo is green and CuSe is pink.

5.5. CIGS Solar Cell

A solar cell was fabricated for each deposition process tested. After the CIGS deposition, the buffer and window layer were deposited. For this work, zinc oxide sulfide (Zn(O,S)) was used as a buffer layer with a thickness of 50 nm, with a window layer of 50 nm i-ZnO and 200 nm of aluminum doped zinc oxide (Al:ZnO). All layers were deposited by RF magnetron sputtering with varying parameters to ensure a stable plasma and a consistent deposition.

To characterize the solar cells, each sample had to be divided into single cells, which was done by scratching a pattern into the cell using a needle. First, a template that divides each sample into 25 cells with an approximate size of 3 mm by 3 mm was made. Then, it was necessary to remove the absorber in one edge with a scalpel to expose the Mo layer, which was covered with a thin layer of elemental In, applied using a soldering iron to prevent Mo oxidation and improve the electrical contact to the Mo back contact. The final solar cells, shown in Fig 5.12, were photographed with a calipers and trough the image was measured the area of each cell using the freeware ImageJ. This final process is necessary since the scratching is done manually and it has a lot of variance from one cell to the other.
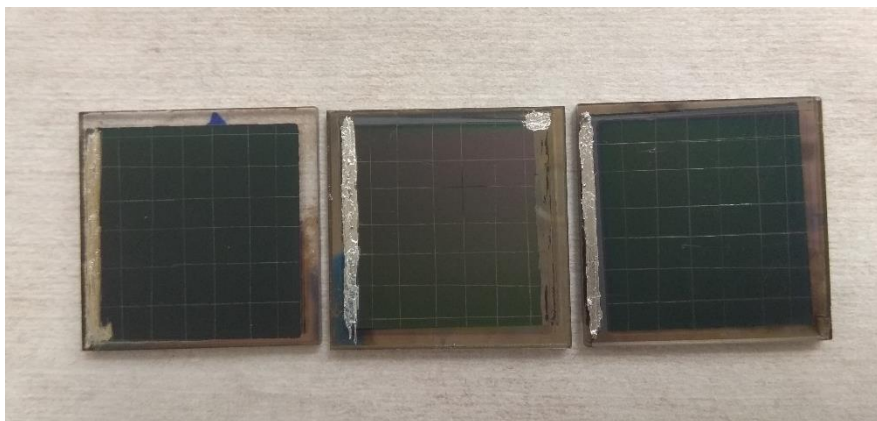
Figure 5.12 – CIGS solar cell devices. CIGS co-deposition (left), CIG deposition with post selenization (middle) and CIGS pulsed deposition (right)

The characterization was carried out at a sun simulator, where the I-V characteristics of the cells is measured using a 4-point-probe set up. The CIGS solar cell prepared by co-deposition presented efficiencies from 0.6 to 1.57% (Fig 5.13 (a)). Figure 5.13 (b) and Table 5.7 show the J-V curve and the characteristics values obtained for cell 2, with the highest efficiency.
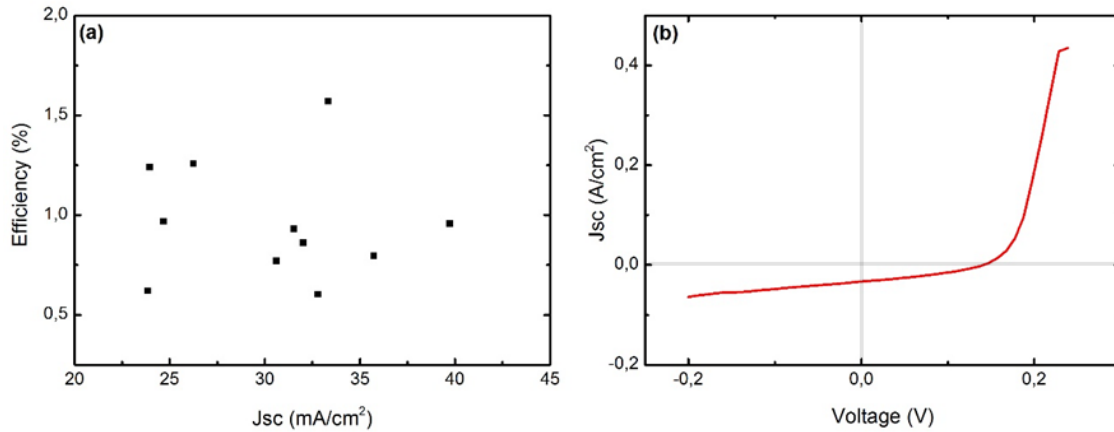
Figure 5.13 – (a) CIGS solar cells prepared by co-deposition efficiencies and (b) J-V curve from cell 2

Tabela 5.7 - Solar cell 2 properties measured at the sun simulator

Sample area (cm²)	0.092
V_{max} **(V)**	0.084
V_{oc} **(V)**	0.14
I_{max} **(A)**	0.0017
I_{sc} **(A)**	0.0031
P_{max} **(mW)**	0.15
Fill Factor	33.87
Efficiency (%)	1.57

The solar cells from the CIG sputtering with post selenization and the CIGS pulsed deposition did not work, therefore, no efficiency was obtained. Both samples had Cu-rich absorber layer ([Cu]/[III] > 1.5) and according to literature [19], devices with a [Cu]/[III] ratio higher than 0.95 do not show any photovoltaic effect.

6. Conclusion and Outlook

The objective of this thesis was to develop a deposition process for Cu(In,Ga)Se$_2$ absorber layer by sputtering using the STAR system. Three depositions processes were tested, (1) CIGS co-deposition, (2) CIG deposition with post selenization and (3) CIGS pulsed deposition.

Although several depositions were performed at STAR, all the CIGS depositions were initiated in this work, therefore an extensive series of depositions were required to understand and calibrate the system. Through the calibration experiments, the Ar and power influence on the film thickness was confirmed, as well as the substrate temperature influence of thickness, surface morphology and chemical composition.

The CIGS co-deposition presented good and consistent results. Although the chemical composition results were different from the one expected according to the target stoichiometry, the [Cu]/[III] ratio values were the desired ones and XRD confirmed the presence of the CIGS tetragonal phase, indicating that the co-deposition are adequate to form CIGS compounds. The solar cell prepared using this process showed an efficiency of 1.57%.

The CIG deposition with post selenization revealed to be an unsuitable deposition process. During the post selenization, the film thickness increases approximately 955 nm, however, the chemical composition of the film modifies and the Cu-poor film becomes Cu-rich. XRD results confirmed the presence of tetragonal CIGS, hexagonal CuSe and tetragonal CuInSe$_2$. Although the reason for this chemical composition change during the selenization is unclear, it is assumed that the amount of Se may be excessive.

Pulsed deposition results were consistent but the process also revealed to be unsatisfactory. In this process, the film chemical composition had the highest [Cu]/[III] ratio, 2.2, indicating a film highly Cu-rich, which was confirmed by XRD with the presence of tetragonal CIGS and hexagonal CuSe.

The deposition processes tested in this thesis showed that the co-deposition process, even not optimized, is the most suitable, presenting consistent and satisfactory results. For future research in CIGS absorber layer more experiments can be done to optimize all the processes, including a more in depth analysis of parameters such as sputtering power and substrate temperature. Another possibility is to vary the Se flow and temperature during the post selenization and pulsed deposition in order to verify the chemical composition variation of the film.

7. References

[1] Hamakawa, Y. (2004). Background and motivation for thin-film solar cell development. In Y. Hamakawa, *Thin-film solar cells: Next generation photovoltaics and its applications* (pp. 1-14). Berlin: Springer.

[2] Roy, N. K., & Das, A. (2018). Prospects of renewable energy sources. In M. R. Islam, N. K. Roy, & S. Rahman, *Renweable energy and the environment*. Singapore: Springer.

[3] Dincer, I. (2000). Renewable energy and sustainable development: a crucial review. *Renewable and Sustainable Energy Reviews*, 4, pp. 157-175.

[4] Kabir, E., Kumar, P., Kumar, S., Adelodum, A. A., & Kim, K.-H. (2018). Solar energy: potential and future prospects. *Renewable and Sustainable Energy Reviews*, 82, pp. 894-900.

[5] Ramanujam, J., & Singh, U. P. (2017). Copper indium gallium selenide based solar cells - a review. *Energy Environmental Science*, 10, p. 1306.

[6] Goetzberger, A., Hebling, C., & Schock, H.-W. (2003). Photovoltaic materials, history, status and outlook. *Materials Science and Engineering*, 40, pp. 1-46.

[7] Chaar, L. E., Iamont, L. A., & Zein, N. E. (2011). Review of photovoltaic technologies. *Renewable and Sustainable Energy Reviews*, 15, pp. 2165-2175.

[8] Shah, A., Torres, P., Tscharner, R., Wyrsch, N., & Keppner, H. (1999). Photovoltaic technology: the case for thin-film solar cells. *Science*, 285, p. 692.

[9] Conibeer, G. (2007). Third-generation photovoltaics. *Materials Today, 10*, p. 42.

[10] Twidell, J., & Weir, T. (2015). *Renewable energy sources.* London and New York: Routledge.

[11] Sen, Z. (2008). *Solar energy fundamentals and modeling techniques: atmosphere, environment, climate change and renewable energy*. London: Springer.

[12] Correia, D. M. (2016). *Development of a micro CuInSe$_2$ solar cell grown by electrodeposition.* Master dissertation, University of Minho, 68 pages.

[13] Chirila, A. *el al.* Highly eficiente Cu(In,Ga)Se$_2$ solar cells grown on flexible polymer films. *Nature materials*, 10, pp 857-861.

[14] Deb, S. K. (2004). Recent advances and future opportunities for thin-film solar cells. In Y. Hamakawa, *Thin-film solar cells: Next generation photovoltaics and its applications* (p. 15). Berlin: Springer.

[15] Lee, T. D., & Ebong, A. U. (2017). A review on thin film solar cell technologies and challenges. *Renewable and Sustainable Energy Reviews*, 70, pp. 1286-1297.

[16] Jackson, P., Hariskos, D., Lotter, E., Paetel, S., Wuerz, R., Menner, R., Powalla, M. (2011). New record efficiency for $Cu(In,Ga)Se_2$ thin-film solar cells beyond 20%. *Progress in Photovoltaics: Research and Applications*, 19, pp. 894-897.

[17] Schock, H.-W; Noufi, R. (2000). CIGS-based solar cells for the next millennium. *Progress in photovoltaics: Research and applications*, 8, pp. 151-160.

[18] Chopra, K. L., Paulson, P. D., & Dutta, V. (2004). Thin-film solar cells: an overview. *Progress in Photovoltaics: Research and Applications*, 12, pp. 69-92.

[19] Konogai, M., & Kushiya, K. (2004). Development of $Cu(In,Ga)Se_2$ thin film solar cells. In Y. Hamakawa, *Thin-film solar cells: Next generation photovoltaics and its applications* (p. 183). Berlin: Springer.

[20] Feurer, T., Reinhard, P., Avancini, E., Bissig, B., Löckinger, J., Fuchs, P., Tiwari, A. (2017). Progress in thin film CIGS photovoltaics - Research and development, manufacturing, and applications. *Progress in photovoltaics: Research and applications*, 25, pp. 645-667.

[21] Schock, H.-W. (2004). Properties of chalcopyrite-based materials and film deposition for thin-film solar cells. In Y. Hamakawa, *Thin-film solar cells: Next generation photovoltaics and its applications* (p. 163). Berlin: Springer.

[22] Shafarman, W. N., Siebentritt, S., & Stolt, L. (2011). $Cu(InGa)Se_2$ Solar Cells. In A. Luque, & S. Hegedus, *Handbook of Photovoltaic Science and Engineering* (Second ed., p. 546). Wiley.

[23] Posada, J., Jubault, M., Bousquet, A., Tomasella, E., & Lincot, D. (2018). Investigations of temperature and power effects on $Cu(In,Ga)Se_2$ thin-film formation during a 3-stage hybrid co-sputtering/evaporation process. *Progress in Photovoltaics: Research and Applications*, 26, pp. 24-37.

[24] Mahan, J. E. (2000). *Physical Vapor Deposition of Thin Films*. New York: Wiley.

[25] Adachi, H., & Wasa, K. (2012). Thin Films and Nanomaterials. In K. Wase, I. Kanno, & H. Kotera, *Handbook of Sputter Deposition Technology* (Second ed.). William Andrew Publisher.

[26] Vossen, J. L., & Cuomo, J. J. (1978). Glow Discharge Sputter Deposition. In J. L. Vossen, & W. Kern, *Thin Film Processes*. San Diego: Academic Press.

[27] Westwood, W. D. (1995). Reactive Sputtering: Introduction and General Discussion. In D. A. Glocker, & S. I. Shah, *Handbook of Thin Film Process Technology*. Bristol: Institute of Physics Publishing.

[28] Adachi, H., Hata, T., & Wasa, K. (2012). Basic Process of Sputtering Deposition. In K. Wasa, I. Kanno, & H. Kotera, *Handbook of Sputter Deposition Technology* (Second ed.). William Andrew Publisher.

[29] Park, N.-M., Lee, H. S., Cho, D.-H., Chung, Y.-D., Kim, K.-H., Lee, K.-S., & Kim, J. (2012). Effect of Se flux on $CuIn_{1-x}Ga_xSe_2$ film in reactive sputtering process. *Progress in Photovoltaics: Research and Applications*, 20, pp. 899-903.

[30] Goldstein, J. I., Newbury, D. E., Michael, J. R., Ritchie, N. W., Scott, J. J., & Joy, D. C. (2018). *Scanning Electron Microscopy and X-ray Microanalysis* (Fourth ed.). New York: Springer.

[31] Baer, D. R., & Thevuthasan, S. (2010). Characterization of Thin Films and Coatings. In P. M. Martin, *Handbook of Deposition Technologies for Films and Coatings* (Third ed.). William Andrew Publishing.

[32] Smith, D. L. (1995). *Thin-Film Deposition: Principles and Practice*. Boston: McGraw-Hill.

[33] Mehta, R. (2012). Interactions, Imaging and Spectra in SEM. *Scanning Electron Microscopy*. (V. Kazmiruk, Ed.) InTech. doi:10.5772/35586

[34] Salvador, P. B. (2016). *Deposition and Caracterization of CdS and ZnO:Al thin films for Cu(In,Ga)Se$_2$ solar cells*. PhD dissertation, University of Minho, 107 pages.

[35] Mattox, D. M. (2010). Non-Elemental Characterization of Films and Coatings. In P. M. Martin, *Handbook of Deposition Technologies for Films and Coatings* (Third ed., p. 716). William Andrew Publisher.

[36] Contreras, Miguel A., et al. "Progress toward 20% efficiency in Cu(In,Ga)Se$_2$ polycrystalline thin-film solar cells." *Progress in Photovoltaics: Research and Applications* 1999: 311-316.

[37] Park, N.-M., Lee, H. S., & Kim, J. (2012). Reactive Sputtering Process for $CuIn_{1-x}Ga_xSe_2$ Thin Film Solar Cells. *ETRI Journal*, 34, p. 779.

[38] Koo, J., Jeon, S., Oh, M., Cho, H.-i., Son, C., & Kim, W. K. (2013). Optimization of Se layer thickness in Mo/CuGa/In/Se precursor for the formation of Cu(InGa)Se$_2$ by rapid thermal annealing. *Thin Solid Films*, 535, pp. 148-153.